Modeling neuron-astrocyte interactions in neural networks using distributed simulation

Han-Jia Jiang[1,2 * ‡], Jugoslava Aćimović[3 * ‡], Tiina Manninen[3], Iiro Ahokainen[3], Jonas Stapmanns[1,4], Mikko Lehtimäki[3], Markus Diesmann[1,4,5], Sacha J. van Albada[1,2], Hans Ekkehard Plesser[1,6,7 ‡], Marja-Leena Linne[3 * ‡]

1 Institute for Advanced Simulation (IAS-6), Jülich Research Centre, Jülich, Germany
2 Institute of Zoology, Faculty of Mathematics and Natural Sciences, University of Cologne, Cologne, Germany
3 Faculty of Medicine and Health Technology, Tampere University, Tampere, Finland
4 Department of Physics, Faculty 1, RWTH Aachen University, Aachen, Germany
5 Department of Psychiatry, Psychotherapy and Psychosomatics, School of Medicine, RWTH Aachen University, Aachen, Germany
6 Department of Data Science, Faculty of Science and Technology, Norwegian University of Life Sciences, Ås, Norway
7 Käte Hamburger Kolleg: Cultures of Research (c:o/re), RWTH Aachen University, Aachen, Germany
‡These authors contributed equally to this work.
* hjiang2@smail.uni-koeln.de, jugoslava.acimovic@tuni.fi, marja-leena.linne@tuni.fi

Abstract

Astrocytes engage in local interactions with neurons, synapses, other glial cell types, and the vasculature through intricate cellular and molecular processes, playing an important role in brain information processing, plasticity, cognition, and behavior. This study aims to enhance computational modeling of local interactions between neurons and astrocytes to better understand how these interactions influence the activity regimes in neuron-astrocyte networks and overall brain function. We develop new algorithms for representing astrocytes and neuron-astrocyte interactions in distributed simulation code for large-scale spiking neuronal networks. These include an astrocyte model with calcium dynamics, an extension of a standard neuron model to receive calcium-dependent signals from astrocytes, connections that deliver these signals to neurons, and a connectivity concept that efficiently establishes interactions between groups of three elements (pre- and postsynaptic neurons and astrocytes) in large neuron-astrocyte populations. The latter extends the conventional concept of binary connectivity in neuronal circuits. We verify the efficiency of our reference implementation through a series of benchmarks that vary in computing resources and neuron-astrocyte network model sizes. Using the new technology, we reproduce experimental data on astrocytic effects on neuronal synchronization. Our *in silico* experiments demonstrate that astrocytes consistently induce local synchronization in groups of neurons across various connectivity schemes and global activity regimes. Changing only the efficiency of neuron-astrocyte interactions switches the global activity regime from asynchronous to network-wide synchronization. Our contribution supports reproducible and collaborative large-scale modeling projects of neuron-astrocyte circuits, addressing the growing interest in developing these models within the computational neuroscience community.

Keywords

astrocyte, computational neural model, NEST simulator, neuron-astrocyte interaction, calcium dynamics, spiking neuronal network, glutamatergic synaptic transmission, spontaneous activity in neural system, synchronization in neuron-astrocyte network, glia, connectivity

Author summary

Astrocytes play an important role in regulating synapses, neuronal networks, and cognitive functions. However, models that include both neurons and astrocytes are underutilized compared to models with only neurons in theoretical and computational studies. We address this issue by developing concepts for the representation of astrocytic interaction and providing a reference implementation in the distributed spiking network simulation code NEST. Using these capabilities, we show how astrocytes help to synchronize neural networks under various connection patterns and activity levels. The new technology makes it easier to include astrocytes in simulations of neural systems, promoting the construction of more realistic, relevant and reproducible models.

Data Availability Statement

The implemented astrocyte support is described in the user-level documentation of the NEST simulation code [1]. Benchmark code and the code for developing and simulating the *in silico* model are available at https://zenodo.org/doi/10.5281/zenodo.13757203. The supporting information (S1 Appendix, S2 Appendix, and S3 Appendix) describe new variables and parameters of the NEST code, the specification of the network models used in this study, and the criteria for the choices of parameter values.

Funding

This research has received funding from the European Union's Horizon 2020 Framework Programme for Research and Innovation under Specific Grant Agreement No. 945539 (Human Brain Project SGA3) to SJvA and M-LL, from its Partnering Project (AstroNeuronNets) to JA and SJvA, from the European Union's Horizon Europe Programme under the Specific Grant Agreement No. 101147319 (EBRAINS 2.0 Project) to SJvA and M-LL, from HiRSE_PS, the Helmholtz Platform for Research Software Engineering - Preparatory Study, an innovation pool project of the Helmholtz Association, to SJvA, from Research Council of Finland, decision Nos. 326494, 326495, 345280, and 355256, to TM, and 297893 and 318879 to M-LL, and from The Käte Hamburger Kolleg: Cultures of Research (c:o/re) which is funded by the Federal Ministry of Education and Research under the funding code 01UK2104 to HEP. Open access publication funded by the Deutsche Forschungsgemeinschaft (DFG, German Research Foundation) – 491111487.

The funders had no role in study design, data collection and analysis, decision to publish, or preparation of the manuscript.

Competing interests

The authors have declared that no competing interests exist.

Introduction

Astrocytes, a prevalent glial cell subtype within the brain, fulfill many roles encompassing the facilitation of synaptic pruning and maturation, regulation of extracellular ionic concentrations, and active participation in metabolic processes as well as the maintenance of the blood-brain barrier. *In vivo*, astrocytes are organized into three-dimensional spatially separated domains with little overlap between domains [2–8]. Each astrocytic domain covers tens to hundreds of thousands of synapses in rodents and even up to millions of synapses in humans [2, 3, 6]. Within their domains, astrocytes ramify into complex morphologies containing multiple processes that are positioned close to synapses (see, e.g., [6, 8]) and maintain bidirectional interactions with synapses [9]. Astrocytes react to released neurotransmitters, including glutamate and gamma-aminobutyric acid (GABA), by elevating their intracellular inositol trisphosphate (IP_3) and calcium levels [10]. Elevated astrocytic calcium levels have been shown to stimulate the release of gliotransmitters, such as glutamate, D-serine, and adenosine triphosphate (ATP) via exocytosis [9–12]. The released gliotransmitters can affect neuronal excitability, for example, the release of glutamate has been shown to induce neuronal extrasynaptic N-methyl-D-aspartate receptor (NMDAR)-mediated slow inward currents (SICs). SICs were first shown in hippocampal neuron-astrocyte co-cultures two decades ago [13], but have since been documented in brain slices of hippocampus and other brain areas as well [14–27], and in humans [28] in addition to rodents.

Computational modeling provides methodology and tools to integrate the knowledge about complex molecular and cellular machinery, cell morphology, and spatial organization of astrocytic domains with electrophysiological and imaging data from neurons and astrocytes into models of large-scale neuron-astrocyte circuits. Such circuit-level models can be used to examine how various molecular and cellular mechanisms affect global dynamical regimes and fundamental functions of brain circuits such as sensory processing, learning, and memory. Furthermore, biologically detailed and data-driven models can be used to probe how specific disease-related dysfunctions on genetic, molecular and cellular levels alter global dynamical regimes in brain circuits and contribute to brain disorders.

In the past two decades, the interest in computational modeling of neuron-astrocyte circuits has been steadily increasing (for review and analysis of models see, e.g., [29–33]). However, published models consider only small networks compared to the extent of the biological interaction and are rarely implemented using standard open-access simulation tools or supplemented with code and extensive documentation in public repositories. This hinders reuse of models and reproducibility of the reported results. To address these challenges, we develop concepts for the representation of neuron-astrocyte interaction in large-scale models and provide a reference implementation for the simulation code NEST [1, 34]. NEST is a widely used open-source, community-developed simulator integrated into the EBRAINS infrastructure. NEST promotes methodological model specification and allows efficient simulation and analysis of realistic-size neural circuits (see, e.g., [35, 36]). Our new development complements the list of a few previous astrocytic implementations in simulators, namely ARACHNE [37] and Brian2 [38, 39], by focusing on simulations of large neural networks facilitated by distributed parallel computing based on Message Passing Interface (MPI). In addition, we introduce new connectivity concepts for the tripartite neuron-astrocyte interactions and develop functions in NEST that implement these concepts. We propose efficient data structures and algorithms for network construction and simulation, combined with domain-specific language constructs supporting the definition of interactions in large heterogeneous neuron-astrocyte models.

The framework comprises a model for astrocytic calcium dynamics [40, 41], a model

for neuron-astrocyte interaction [42], and a method for pairing synapses with astrocytes in neuron-astrocyte circuits. We extend the concept of a synapse, conventionally composed of a presynaptic and a postsynaptic component, with an astrocyte element and develop respective modeling language constructs for tripartite connectivity. The new language constructs allow researchers to complement probabilistic connections rules for neuron populations with specifications for connections with a third factor, such as an astrocyte population. In this framework, we implement neuron-astrocyte interactions through glutamatergic signaling and SICs, based on a previously published model [42] already used in several follow-up studies (see, e.g., [32, 43, 44]). We verify the efficiency of the data structures and algorithms through a series of benchmarks of the reference implementation in NEST by evaluating the computational load associated with different steps in the simulation while systematically scaling up computing resources and model size. The benchmarks show that the implementation provides an efficient tool for large-scale modeling of neuron-astrocyte circuits.

Next, we demonstrate the capability of the new technology to serve as a platform for *in silico* experiments on neuron-astrocyte circuits. Recent experimental evidence reveals coordinated activity of astrocytic and neuronal populations *in vitro* [45] and *in vivo* in behaviorally relevant tasks [46]. Here, we explore a specific mechanism, the emergence of coordinated neuronal and astrocytic activity through the release of glutamate from astrocytes, that induces SICs in postsynaptic neurons. In the central nervous system, SICs contribute to the synchronization of neurons in close proximity, thereby influencing the coordination of local network activity [15, 16, 21, 47]. Additionally, large SICs in cortical areas may hold pathophysiological implications, as they can synchronize neuronal network activity and facilitate the generation of seizures [19, 48], contributing to the pathophysiology of stroke and cerebral edema [27, 49]. Moreover, according to very recent findings, SICs are likely to play an important role in age-dependent physiological and pathological alterations of brain activity in humans, including synaptic plasticity [50]. Brainstem SICs may serve different functions, as previous research [24, 51] has not identified widespread synchronization of these events among neighboring neurons.

We note that SICs exhibit slower kinetics than spontaneous or miniature excitatory postsynaptic currents. The prevailing view is that GluN2B-containing NMDARs drive the generation of SICs [15, 16, 20, 21, 23, 47, 52]. This disparity in kinetic and dynamical properties affects the emergence of coordinated activity in neuron-astrocyte systems.

We construct a spiking neuron-astrocyte network model comparable to a selected experimental study [47, 52] and use it to show that astrocytes robustly enhance neuronal synchrony *in silico* for diverse network activity regimes and connectivities. We fit the parameters of an astrocyte model to reproduce frequency and duration of spontaneous calcium transients reported in the literature [45, 53–55]. The first set of *in silico* experiments distributes neurons across non-overlapping domains, where all neurons in the same domain interact with the same one astrocyte. When synaptic transmission between neurons is suppressed, astrocytes promote synchronized activity among neurons within their respective domains, aligning with experimental findings. In models where neurons fire at biologically realistic frequencies, astrocytes still induce synchrony within their domains, both in a low-rate asynchronous network spiking regime and in the presence of network-wide bursts. Switching from low-rate asynchronous spiking to network-wide bursting is achieved by increasing the strength of inputs from neurons to astrocytes. The bursting regime induces some degree of synchrony between the majority of neurons in the model, still the synchrony within domains remains significantly above the level of synchrony in the whole network. In the second set of experiments, neurons typically belong to more than one astrocytic domain and interact with more than one astrocyte. Therefore each neuron can belong to more than one synchronous group. We

show that, in this case as well, the synchronization within domains still exceeds overall synchronization in the network.

The structure of the present work is as follows. We first provide the details of the astrocyte framework including the user interface in Methods. We then verify the efficiency of our reference implementation in Results, confirming that it can serve as a platform for the study of large-scale neuron-astrocyte circuits. Finally, we demonstrate how the new capabilities can be used to reproduce and extend experimental studies.

Preliminary results of this study have appeared in abstract form [56, 57]. The technology described in the present article has been released as open source with several major releases of NEST. The conceptual and algorithmic work is a module in our long-term collaborative project to provide the technology for neural system simulations [34].

Methods

Data structures and algorithms for neuron-astrocyte interaction

The model of neuron-astrocyte interaction we consider in this work has four components: **(a)** a Li-Rinzel astrocyte model (`astrocyte_lr_1994`) with calcium dynamics [40, 41], and a mechanism that generates a calcium-dependent SIC [42], **(b)** an extended AdEx neuron model (`aeif_cond_alpha_astro`) capable of receiving the SIC elicited by astrocytes, **(c)** `sic_connection` for transmitting time-continuous SIC signal efficiently from astrocytes to neurons also in parallel simulations, and **(d)** a tripartite connection rule (`TripartiteConnect()`) extending the standard notion of (binary) connectivity in neuronal circuits by allowing to establish interactions between triplets of elements facilitating parallel construction of networks including astrocytes. The biological mechanisms modeled with this implementation are illustrated in Fig 1.

The reference code contains implementations of the astrocyte and neuron models and the SIC interaction starting with release NEST 3.6 [58] and a preliminary version of the tripartite connectivity concept from NEST 3.7 [59], while the definite version of the tripartite concept appears from NEST 3.8 [1]. A fourth component solely for the purpose of benchmarks presented here is a simplified variant of the astrocyte model. This is not integrated into the NEST code base but provided as an extension module on GitHub [60]. The remainder of this section describes each of these components and gives a reference implementation. Model documentation and example scripts are available through Read the Docs. Nordlie tables [61] summarize the model equations in S1 Appendix.

The present work requires a two-step mapping of notation. In the first, the mathematical notation of a range of studies needs to be unified to interrelate the components of the network models. In the second, the unified notation needs to be mapped to a domain-specific programming language for expressing the models in executable descriptions. An ontology of variables and parameters together with their default values is given in S2 Appendix. The phenomenological models of the present study, based on phenomenological description of biological mechanisms and the abstractions of the anatomy, require parameter fitting to the experimental data from the literature. These procedures are detailed in S3 Appendix.

Astrocyte model

We implement an astrocyte model `astrocyte_lr_1994` according to the Li-Rinzel reduction [41] of the De Young-Keizer model [40] for intracellular calcium dynamics in nonexcitable cells. The Nadkarni-Jung model extends the Li-Rinzel model by adding

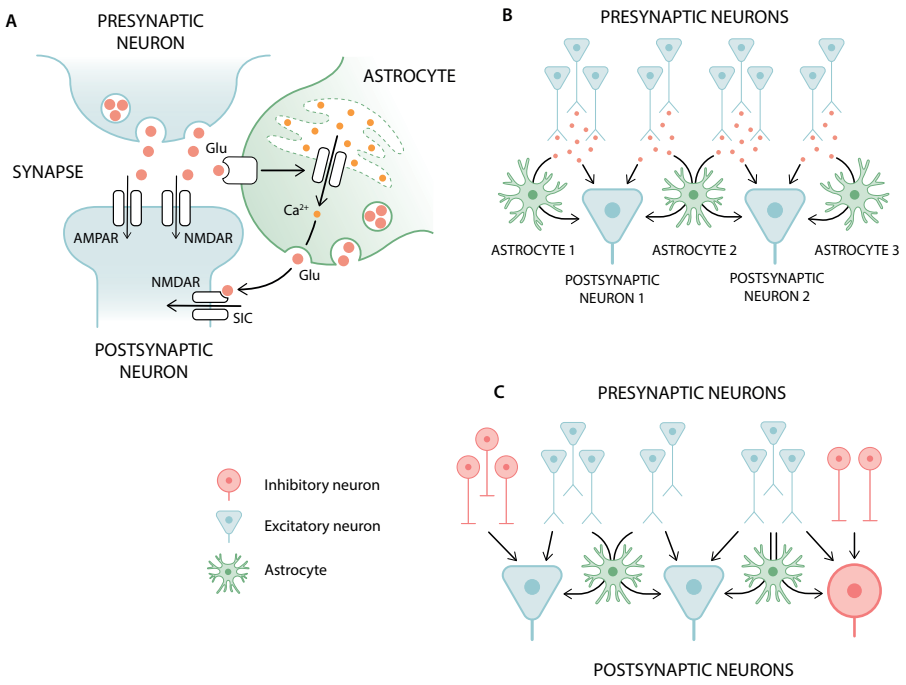

Fig 1. Illustration of the biological mechanisms captured by the model framework for astrocytes. (A) Feed-forward interaction from the presynaptic neuron to the postsynaptic neuron: direct synaptic exchange and an indirect pathway through a neighboring astrocyte. This interaction with an astrocyte is modeled only for the glutamatergic synapses while GABAergic synapses include only interaction between the two neurons. (B) Interaction scheme between astrocytes and excitatory neurons. An astrocyte receives glutamate from all its presynaptic contacts and induces slow inward currents (SICs) only in those postsynaptic neurons that form synapses with its presynaptic contacts. (C) Extension of the interaction scheme in B by inhibitory neurons. Astrocytes are only involved in excitatory-excitatory and excitatory-inhibitory connections.

astrocytic input and output mechanisms [42]. Our implementation follows the published equations [41, 42] with further adaptations of inputs and outputs. All parameter values are given in S2 Appendix. Here, we provide an overview of the model structure.

Input to the astrocyte induces the production of astrocytic IP_3, and the change in IP_3 concentration ($[IP_3]$) affects the flux of calcium from the endoplasmic reticulum (ER) to the cytosol through the IP_3 receptor (IP_3R) channel. The cytosolic calcium concentration ($[Ca^{2+}]$) determines the output of the astrocyte, which is a SIC to its target neurons. These mechanisms are illustrated in Fig 1A. The equations for the astrocytic dynamics are:

$$\frac{d[\mathrm{Ca}^{2+}](t)}{dt} = J_{\mathrm{channel}}(t) - J_{\mathrm{pump}}(t) + J_{\mathrm{leak}}(t) + J_{\mathrm{noise}}(t), \tag{1}$$

where

$$\begin{aligned}
J_{\mathrm{channel}}(t) &= r_{\mathrm{ER,cyt}} \cdot v_{\mathrm{IP_3R}} \cdot m_\infty^3(t) \cdot n_\infty^3(t) \cdot h_{\mathrm{IP_3R}}^3(t) \cdot \left([\mathrm{Ca}^{2+}]_{\mathrm{ER}}(t) - [\mathrm{Ca}^{2+}](t)\right), \\
m_\infty(t) &= \frac{[\mathrm{IP_3}](t)}{[\mathrm{IP_3}](t) + K_{\mathrm{d,IP_3,1}}},\ n_\infty(t) = \frac{[\mathrm{Ca}^{2+}](t)}{[\mathrm{Ca}^{2+}](t) + K_{\mathrm{d,act}}}, \\
\frac{dh_{\mathrm{IP_3R}}(t)}{dt} &= \alpha_h(t) \cdot (1 - h_{\mathrm{IP_3R}}(t)) - \beta_h(t) \cdot h_{\mathrm{IP_3R}}(t), \\
\alpha_h(t) &= k_{\mathrm{IP_3R}} \cdot K_{\mathrm{d,inh}} \cdot \frac{[\mathrm{IP_3}](t) + K_{\mathrm{d,IP_3,1}}}{[\mathrm{IP_3}](t) + K_{\mathrm{d,IP_3,2}}},\ \beta_h(t) = k_{\mathrm{IP_3R}} \cdot [\mathrm{Ca}^{2+}](t), \\
J_{\mathrm{pump}}(t) &= \frac{v_{\mathrm{SERCA}} \cdot [\mathrm{Ca}^{2+}]^2(t)}{K_{\mathrm{m,SERCA}}^2 + [\mathrm{Ca}^{2+}]^2(t)}, \\
J_{\mathrm{leak}}(t) &= r_{\mathrm{ER,cyt}} \cdot v_{\mathrm{L}} \cdot \left([\mathrm{Ca}^{2+}]_{\mathrm{ER}}(t) - [\mathrm{Ca}^{2+}](t)\right).
\end{aligned}$$

J_{channel}, J_{leak}, and J_{pump} are the three terms determining the flux of calcium between cytosol and ER. J_{channel} is the IP_3R-mediated release of calcium from the ER to the cytosol, J_{pump} refers to the ATP-dependent transport of calcium to the ER via the sarco/ER calcium-ATPase (SERCA), and J_{leak} is the leak of calcium between the ER and cytosol. In addition to these standard terms, we include the term $J_{\mathrm{noise}}(t)$ to account for random fluctuations in calcium dynamics.

The parameters and variables involved in Eq (1) are as follows. $r_{\mathrm{ER,cyt}}$ is the ratio between astrocytic ER and cytosol volumes. $v_{\mathrm{IP_3R}}$ is the maximum rate of calcium release via astrocytic IP_3Rs. $K_{\mathrm{d,IP_3,1}}$ and $K_{\mathrm{d,IP_3,2}}$ are the first and second astrocytic IP_3R dissociation constants of IP_3. $K_{\mathrm{d,act}}$ and $K_{\mathrm{d,inh}}$ are the astrocytic IP_3R dissociation constants of calcium (for activation and inhibition, respectively). $k_{\mathrm{IP_3R}}$ is the astrocytic IP_3R binding constant for calcium inhibition. v_{SERCA} is the maximum rate of calcium transport by astrocytic SERCA pumps. $K_{\mathrm{m,SERCA}}$ is the half-activation constant of astrocytic SERCA pumps. v_{L} is the rate constant of calcium leak from astrocytic ER to cytosol. $[\mathrm{Ca}^{2+}]_{\mathrm{ER}}$ is the calcium concentration in the ER. $m_\infty(t)$ and $n_\infty(t)$ are steady-state values for two gating variables of IP_3Rs. $h_{\mathrm{IP_3R}}(t)$ is the fraction of IP_3Rs that are not yet inactivated by calcium. $\alpha_h(t)$ and $\beta_h(t)$ are two rates of the exchange between activated and inactivated IP_3Rs.

In addition, the total amount of calcium in the astrocyte (cytosol + ER), is kept constant:

$$[\mathrm{Ca}^{2+}]_{\mathrm{ER}}(t) = \frac{\mathrm{Ca_{tot}} - [\mathrm{Ca}^{2+}](t)}{r_{\mathrm{ER,cyt}}},$$

where $\mathrm{Ca_{tot}}$ is the parameter determining the maximal cytosolic calcium concentration, i.e., the cytosolic calcium concentration given that all the calcium ions are in the cytosol (see [40] for details).

The astrocyte receives presynaptic spike events as excitatory inputs, similarly to previous studies [37, 39], which initiate IP_3 production given by

$$\frac{d[\mathrm{IP}_3](t)}{dt} = \frac{[\mathrm{IP}_3]_0 - [\mathrm{IP}_3](t)}{\tau_{\mathrm{IP}_3}} + \Delta_{\mathrm{IP}_3} \cdot J_{\mathrm{syn}}(t), \tag{2}$$

where $[\mathrm{IP}_3]_0$ is the baseline value of $[\mathrm{IP}_3]$, τ_{IP_3} is the time constant of the exponential decay of $[\mathrm{IP}_3]$, Δ_{IP_3} is the parameter determining the increase in $[\mathrm{IP}_3]$ induced by the input, and $J_{\mathrm{syn}}(t)$ is the sum of all excitatory synaptic inputs that the astrocyte receives at time t.

The output of the astrocyte is a SIC to its targets. This current is determined by $[\mathrm{Ca}^{2+}]$ with the phenomenological expression [42], given by

$$I_{\mathrm{SIC}}(t) = a_{\mathrm{SIC}} \cdot \Theta\left(\log(c_{\mathrm{scaled}}(t))\right) \cdot \log(c_{\mathrm{scaled}}(t)), \tag{3}$$

where

$$c_{\mathrm{scaled}}(t) = \left([\mathrm{Ca}^{2+}](t) - \theta_{\mathrm{SIC}}\right)/\mathrm{nM},$$

$\Theta(\cdot)$ is the Heaviside function, and SIC is generated ($I_{\mathrm{SIC}} > 0$) when the calcium concentration is larger than $\theta_{\mathrm{SIC}} + 1$ nM. Our implementation allows the users to change θ_{SIC} in this equation, and specify a factor a_{SIC} to scale the generated SIC. These implementation choices add flexibility to Eq (9) in the original publication [42], where the parameters θ_{SIC} and a_{SIC} are fixed. Here, we use the notation with /nM to indicate that c_{scaled} is the dimensionless version of the given concentration in nM.

SIC-receiving neuron model

Next to a mathematical model of an astrocyte, we need a model of single neuron dynamics susceptible to the SICs astrocytes induce in a neuron. For the purpose of the present work, our starting point is the AdEx neuron model with conductance-based synapses [62, 63]. An additional current (I_{SIC}) in the differential equation describing the membrane potential represents the summed input from all connected astrocytes. The adapted equation of the combined model (`aeif_cond_alpha_astro`) reads

$$C_{\mathrm{m}} \frac{dV(t)}{dt} = F\left(V(t)\right) - W(t) + I_{\mathrm{syn}}(t) + I_{\mathrm{SIC}}(t), \tag{4}$$

where C_{m} is the membrane capacitance, $V(t)$ is the membrane potential, $F\left(V(t)\right)$ defines the passive properties and the spiking mechanism, $W(t)$ is the adaptation variable, $I_{\mathrm{syn}}(t)$ is the summed synaptic current to the neuron, and $I_{\mathrm{SIC}}(t)$ is the summed SIC induced by all connected astrocytes. $F\left(V(t)\right)$ and $W(t)$ follow Eqs (2) and (3) in [62] respectively, and $I_{\mathrm{syn}}(t)$ is given by

$$I_{\mathrm{syn}}(t) = -g_{\mathrm{exc}}(t) \cdot (V(t) - E_{\mathrm{exc}}) - g_{\mathrm{inh}}(t) \cdot (V(t) - E_{\mathrm{inh}}),$$

where g_{exc} and g_{inh} are the summed excitatory and inhibitory synaptic conductances, and E_{exc} and E_{inh} are the excitatory and inhibitory reversal potentials.

When $V(t)$ reaches the spike detection threshold V_{peak}, the reset condition is applied:

$$V(t) = V_{\mathrm{reset}}, \;\; W(t) = W(t^-) + b,$$

where V_{reset} is the reset value for V after a spike, and b is the spike-triggered adaptation. $V(t) = V_{\mathrm{reset}}$ is maintained for a refractory period t_{ref}.

Fig 1B illustrates a situation where an excitatory neuron receives a SIC from two astrocytes, while astrocytes receive inputs from several excitatory presynaptic neurons. Fig 1C extends Fig 1B by adding also inhibitory cells.

SIC connection model

SIC connection is implemented as an unidirectional interaction from the source astrocyte to the target neuron. The connection is dependent on two parameters, the weight that defines the strength of interaction and the connection delay. The interaction is continuous and dependent on the state of the source astrocyte, but independent of the state of the target neuron. This combination of features distinguishes SIC connections from other cell-to-cell interactions available in NEST, such as synaptic connections or gap junctions. Therefore, simulation codes for neuron-astrocyte networks require specific software support for the interaction through SIC, and mathematical models of neuronal networks need to specify this type of interaction if desired. In the present work this interaction is specified as `sic_connection`.

Concepts of tripartite connection rule

The recent review of connectivity concepts in the computational neuroscience literature by Senk et al. [64] concentrates on the connection patterns between two populations of neurons and presents an ontology. The simulation code NEST, for example, provides an implementation for the full set of these concepts. However, neuron-astrocyte networks establish a three-party connectivity. This suggests an interdependence in the connections among three network nodes that goes beyond pairwise probabilities, highlighting innate network motifs in this type of connectivity. A motif is a common graph-theoretic concept extensively used to describe networks with complex connectivity, including neuronal networks [32, 65–68].

In our models, three-node feed-forward motifs are created as follows. Given source and target neuron populations, the primary connection rule selects specific source-target neuron pairs and establishes primary connections between the source and target neuron. For each source-target pair selected, the tripartite connectivity rule then determines whether to attach an astrocyte to the pair. Attachment means that a further connection is created from the source neuron to the astrocyte, and a `sic_connection` is created from the astrocyte to the target neuron.

Even though recent experimental and modeling studies have started to reveal the complexity in the anatomical structure of neuron-astrocyte circuits [5–8], details of this structure in different tissues, brain regions, and organisms are still debated. We therefore provide three alternative statistical descriptions of the structure of neuron-astrocyte connectivity to enable explorative investigations and to support further theoretical analysis of these concepts.

The selection of the specific astrocyte to attach to a given source-target pair is based on *astrocyte pools*, i.e., subsets of the astrocyte population. Fig 2 illustrates alternative pool types and resulting connection patterns. Each neuron in the target population is assigned a fixed astrocyte pool of size `pool_size`. For `pool_type = "random"`, the members of the pool are selected at random from the entire astrocytic population (without replacement). Any given astrocyte can be part of the pools of multiple target neurons and pools assigned to different target neurons typically share some members as illustrated in Fig 2A. This random pool formation corresponds to the *random fixed in-degree without multapses connection rule* as defined by Senk et al. [64], albeit for potential, not actual synapses. Alternatively, choosing `pool_type = "block"` and `pool_size = 1`, assigns exactly one astrocyte to each target neuron, but each astrocyte can interact with more than one target neuron, as shown in Fig 2B. Under this rule and pool size, the number of target neurons needs to be a multiple of the number of astrocytes. Finally, for `pool_type = "block"` and `pool_size > 1`, each target neuron selects exactly `pool_size` astrocytes but these pools do not overlap. The total population of astrocytes needs to be `pool_size` times larger than the number of target

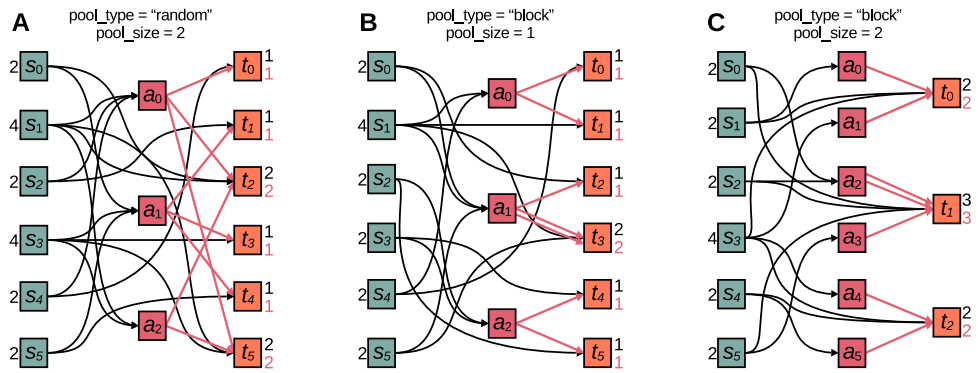

Fig 2. Examples of tripartite neuron-astrocyte connectivity created with NEST support. (A) `pool_type` is random. Each postsynaptic neuron can interact with up to `pool_size` random astrocytes. (B) `pool_type` is `"block"` and `pool_size` is one. Each postsynaptic neuron can interact with one astrocyte. The number of postsynaptic neurons has to be a multiple of the number of astrocytes. (C) `pool_type` is `"block"` and `pool_size` is larger than one. Each postsynaptic neuron can interact with up to `pool_size` astrocytes. The number of astrocytes has to be `pool_size` times the number of postsynaptic neurons. s_0, s_1, ... : presynaptic (source) neurons. t_0, t_1, ... : postsynaptic (target) neurons. a_0, a_1, ... : astrocytes. Black and magenta arrows indicate connections from neurons and astrocytes, respectively. Numbers in front of and behind the neurons indicate numbers of connections from or to them, respectively. The diagram and notations follow the style suggested for neuronal network modeling in [64].

neurons. Fig 2C shows an example where the astrocyte pool is twice as big as the number of target neurons.

Our concrete use case shows that three-node network motifs may exhibit a wide range of patterns in the existence and decoration of their edges. It is beyond the scope of the present work to derive a generic concept for the representation of such connectivity. Therefore we restrict the formalization of three-node network motifs to connectivity induced by astrocytes as described above. Following the analysis of [64], Fig 3 shows a declarative population-level description.

Future work can generalize this concept as further higher-order structures are discovered. The concept specifies three populations of network elements and three sets of parameters, called `syn_specs`, for the edges of the motif. The specification of two connection rules introduces a hierarchy among the edges. The first (`conn_spec`) corresponds to the regular specification of the connection between network elements of two populations as formalized in [64]. The second (`third_pop_conn_spec`) is only relevant if the first actually creates a connection between a pair of network elements from the pre- and the postsynaptic populations, and determines the motif formed with an element of the third population.

Implementation of a tripartite connection rule

The original `Connect()` function in NEST only creates connections between two populations. Therefore, we extend this function to enable the creation of three-party connectivity for neuron-astrocyte networks as described above. Most pairwise connection rules in the ontology of [64] are valid arguments for the primary connection rule, while NEST so far implements only a single third-factor rule: `third_factor_bernoulli_with_pool`.

```
TripartiteConnect(
    prePopulation, postPopulation, thirdPopulation,
    conn_spec={"rule": ...},
    third_pop_conn_spec={
        "rule": ...,
        "pool_size": ...,
        "pool_type": ...},
    syn_specs={
        "primary": ...
        "third_in": ...
        "third_out": ...})
```

Fig 3. Declarative concept of a tripartite connectivity. Pseudocode similar to the Python programming language interface of the reference code NEST. Named parameters in red indicate application specific fields. The concept refers to three populations of network elements. Two rules (`conn_spec` and `third_pop_conn_spec`) express a hierarchy, where the second is only applied if the first actually creates a connection. The nature of the three possible connections (`primary`, `third_in`, `third_out`) can be freely assigned.

To achieve memory- and time-efficient representation and creation of connectivity, NEST generates and stores connectivity on the postsynaptic side, i.e., on the virtual process (VP) managing the target neuron of a connection [69–71]. This causes complications when creating three-party connectivity, since the third node selected may be managed by a different VP than the primary target. We solve this as follows: When the VP managing the target neuron has decided to create a primary connection, it also decides whether to create a third-factor connection and creates the "third out" connection from third-factor node to primary target immediately. It then stores the node ID of the primary source neuron and the selected third-factor node in a buffer local to the VP. Once connection creation of primary and "third out" connections is completed, all VPs exchange the buffered primary source-third-factor pairs and each VP then creates "third in" connections from the selected primary sources to the third-factor nodes it manages. This approach allows for a flexible combination of primary and third-factor connection rules and preserves the scaling properties of the primary connection rule. The algorithm adds an overhead for three-party connectivity that is linear in the number of primary connections and incurs only a single round of inter-process communication for the exchange of source-third-factor pairs.

On a more technical level, we rename the existing NEST `ConnBuilder` base class to `BipartiteConnBuilder`. Each primary connection rule corresponds in NEST to a derived class of `BipartiteConnBuilder`, with responsibility for choosing source-target pairs and creating and parameterizing synapses according to user-provided specifications. To support third-factor connectivity, we further derive from `BipartiteConnBuilder` the classes `ThirdInBuilder` and `ThirdOutBuilder`. `ThirdInBuilder` manages the creation of connections from primary sources to third-factor nodes; since these connections are predetermined by the decisions of `ThirdOutBuilder`, no further sub-classing is allowed. `ThirdOutBuilder`, on the other hand, needs to be sub-classed for each third-factor connection rule. At present, `ThirdBernoulliWithPoolBuilder` is the only such class.

Primary and third-factor builders are combined in a new `ConnBuilder` class, which holds pointers to a builder for the primary connections which must always be present, and optionally pointers to a `ThirdInBuilder` and a `ThirdOutBuilder` which must either both be absent (normal bipartite connectivity) or both be present (tripartite connectivity). Each `BipartiteConnBuilder` holds a pointer to a `ThirdOutBuilder` (null if only bipartite). This allows the primary connection builder to trigger the check

for a third-factor connection for every primary connection created by calling `ThirdOutBuilder::third_connect()`. The `ThirdOutBuilder` in turn holds a pointer to a `ThirdInBuilder`, so that for each "third out" connection created, the `ThirdOutBuilder` can call `ThirdInBuilder::register_connection()` to inform the latter about the primary source-third factor node pair that needs to be connected. The `ThirdInBuilder` maintains two closely connected data structures to manage these pairs: (1) a buffer storing tuples consisting of the global node IDs of the source and the third-factor node, and the MPI rank which manages the third-factor node, and (2) an array of counters recording how many source-target pairs need to be transmitted to each MPI rank. In order to allow for collision-free updating of these data structures during multi-threaded connectivity generation, a separate buffer and set of counters is maintained for each thread within an MPI process.

When the `Connect()` or `TripartiteConnect()` functions in NEST are called, the simulation kernel first creates a `ConnBuilder` instance with a `BipartiteConnBuilder` instance representing the primary connection rule and, for tripartite connectivity, a `ThirdInBuilder` and a `ThirdOutBuilder` instance. It then calls the `connect()` method on the primary connection builder, which creates all connections prescribed by the primary rule and triggers the `ThirdOutBuilder` as required to create the third-out connections. Once this method returns, the `connect_()` method is called on the `ThirdInBuilder`. It first determines locally on each MPI rank the largest number of source-third pairs that needs to be sent to any other rank. This number is shared with all MPI ranks, so that each rank then can determine the globally largest number of pairs to be sent from any rank to any other rank, and transmission buffers are resized correspondingly and filled with local data. Using `MPI_Alltoall()`, pairs are then exchanged between ranks. Afterwards, on any given rank, all source-third pairs are available for which the rank manages the third factor node. Each rank then creates the prescribed connections in thread-parallel fashion, completing the connection process.

The presently implemented `third_factor_bernoulli_with_pool` rule is implemented as class `ThirdBernoulliWithPoolBuilder`. Further third-party rules can be added as new classes. For the implemented class, when the `third_connect()` method is called with a given primary connection, it first performs a Bernoulli experiment with given probability to determine whether to create a third-factor connection. If so, the astrocyte pool for the current target neuron is determined: For block-type pools, pool members are found by suitable indexing into the astrocyte population. For random pools, the pool is created when a given target neuron is connected to an astrocyte for the first time. The third-factor target node is then chosen from the pool with uniform probability, the "third out" connection created and the source-third pair registered with the `ThirdInBuilder`.

With the concepts, rules, and parameters of the algorithms described above, we now concretize the concept of three-party connectivity. This turns the skeleton in Fig 3 into a user interface. In the example in Fig 4, a Bernoulli trial with a given probability (`p`) determines whether the algorithm creates a connection between a pair of neurons from the two primary populations. If this is the case, another Bernoulli trial with an independent parameter (`p`) determines if the primary pair forms a motif with an astrocyte of the third population. In addition, two parameters `pool_type` and `pool_size` restrict the pool of available astrocytes: `pool_size` specifies the size of the pool and `pool_type` requests a random (`"random"`) selection of pool members, in contrast to the selection in blocks (`"block"`). Finally, `syn_specs` specifies models and their parameters for the three edges of the motif. The example uses a specific model of an astrocyte encoded as `astrocyte_lr_1994`, and the communication with astrocytes requires a specific neuron model encoded as `aeif_cond_alpha_astro`. Future studies can introduce further models using the same interface.

```
astrocytes = nest.Create(
    "astrocyte_lr_1994", 100, {"Ca_tot": 2.0, "IP3_0": 0.16})

pre_neurons = nest.Create(
    "aeif_cond_alpha_astro", 100, {"E_L": -70.6, "V_th": -50.4})

post_neurons = nest.Create(
    "aeif_cond_alpha_astro", 100, {"E_L": -70.6, "V_th": -50.4})

nest.TripartiteConnect(
    pre_neurons, post_neurons, astrocytes,
    conn_spec={"rule": "pairwise_bernoulli", "p": 0.1},
    third_factor_conn_spec={
        "rule": "third_factor_bernoulli_with_pool",
        "p": 0.5,
        "pool_size": 10,
        "pool_type": "random"},
    syn_specs={
        "primary": {"synapse_model", "tsodyks_synapse", "weight": 0.7}
        "third_in": {"synapse_model", "tsodyks_synapse", "weight": 0.3}
        "third_out": {"synapse_model", "sic_connection", "weight": 1.0}})
```

Fig 4. Example of tripartite connectivity concept. Pseudocode as in Fig 3. Red indicates application specific fields and symbolic parameter values. The executable description specifies a network of neurons and astrocytes.

Benchmark methods

We evaluate the performance of our reference implementation for astrocytes by simulating neuron-astrocyte network models with NEST and beNNch, a framework for reproducible benchmarks of neuronal network simulations [72]. beNNch measures the scaling of simulation time with number of VPs or compute nodes used. The metrics for performance is the wall-clock time spent on "network creation", "network connection", and "state propagation". "network creation" and "network connection" capture the time spent on creating and connecting cells and recording devices, respectively. "state propagation" captures the time required to advance the dynamical state of the network by the requested span of biological time in the model [72].

All benchmarks use neuron-astrocyte network models in which the ratio of excitatory to inhibitory neuron numbers is 4:1, the ratio of neuron to astrocyte cell numbers is 1:1, and a sparse and random connectivity is established with `TripartiteConnect()` with the `"random"` astrocyte pool type. In the first set of benchmarks, models with different levels of activity or components are compared. The pairwise Bernoulli rule [64] is used to create model connectivity in this set of benchmarks. A model with sparse activity (the "sparse" model) and another with synchronous activity (the "synchronous" model) are created by tuning several model parameters, while NEST defaults are used for the other parameters (see Table B in S1 Appendix). Fig 5 shows the dynamics of these two benchmark models. We compare the benchmark results of these two models in order to demonstrate the effect of model activity.

In order to measure the cost of integrating complex astrocyte dynamics given by Eqs (1)–(3) on the run time of a simulation we define an `astrocyte_surrogate` model. The surrogate model is a copy of the `astrocyte_lr_1994` model, however it neither includes astrocytic dynamics nor processes incoming spikes. It can only emit a continuous, user-configurable and constant SICs to its targets. Therefore, it serves as a surrogate that gives the same type of output as the astrocyte but costs minimum computing resources. We create a benchmark model called "surrogate" that has the same parameters as the "sparse" model but replaces `astrocyte_lr_1994` with `astrocyte_surrogate`. We compare the benchmark results of the "surrogate" model

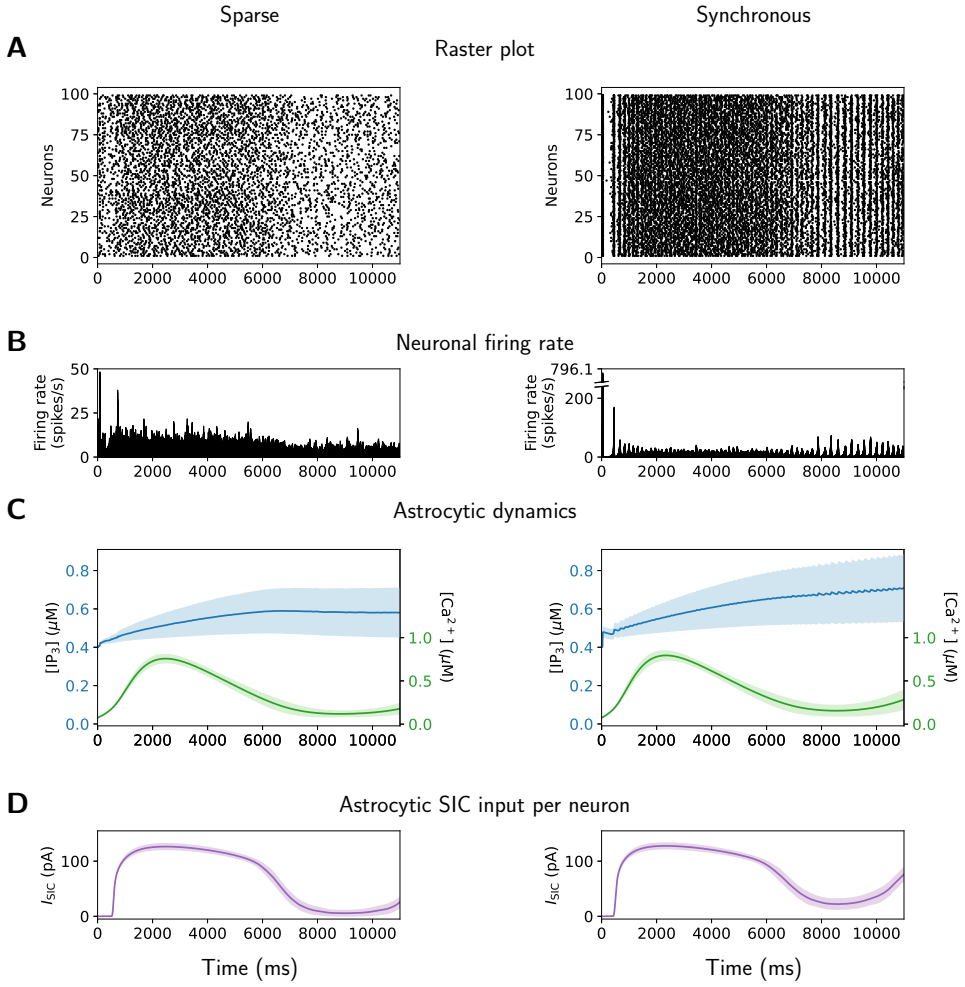

Fig 5. Dynamics of the "sparse" and "synchronous" models used for benchmarks. (A) Raster plot of neuronal firings. (B) Neuronal firing rate. (C) Astrocytic [IP_3] and [Ca^{2+}]. (D) Astrocytic SIC input (I_{SIC}) per neuron. Shaded areas: standard deviations across cells. The left column shows a simulation with the "sparse" model, where the mean neuronal firing rate is 4.74 spikes/s (calculated for 10,000 simulated neurons) and the mean pairwise spike count correlation of sampled neurons is 0.014 (calculated for 100 sampled neurons, bin width = 10 ms). The right column shows a simulation with the "synchronous" model, where the mean neuronal firing rate is 12.0 spikes/s (calculated for 10,000 simulated neurons) and the mean pairwise spike count correlation of sampled neurons is 0.072 (calculated for 100 sampled neurons, bin width = 10 ms). Data from $t = 1$ to $t = 11$ s of the simulation are used for the calculation of firing rate and correlation. For the specifications of the models, see Tables A and B in S1 Appendix. The examples shown here are the case of scale = 1, i.e., number of cells (neurons + astrocytes) is 20,000. The data shown are (A) the first 100 neurons, (B) all neurons, and (C,D) 100 randomly sampled neurons or astrocytes.

with the "sparse" model in order to reveal the cost for the calculation of astrocytic dynamics in the network. In the "surrogate" model, the pre-defined SIC output of `astrocyte_surrogate` is set to such value that the overall neuronal firing rate is close to the "sparse" model. This avoids the confounding caused by different neuronal firing rates.

The second set of benchmarks compares the performance across four connectivity rules: pairwise Bernoulli, fixed in-degree, fixed out-degree, and fixed total number. For specifications of these rules, see [64]. These rules have been developed for neuronal connectivity in earlier versions of NEST, and are now used in `TripartiteConnect()` as the rule for the primary connections in the tripartite connectivity (see Concepts of tripartite connection rule). With this, benchmarks with four versions of the "sparse" model that use the four mentioned rules as the primary connection rule are performed, while keeping the same expected number of connections. The other parameters of these four models are the same as the "sparse" model.

The third set of benchmarks compares the performance for different values of `pool_size`, which specifies the upper bound for the number of astrocytes that each neuron can receive input from. The models used in this set of benchmarks are versions of the "sparse" model with `pool_size` of 10, 100, 1,000, and 10,000.

As in [72], we perform strong and weak scaling benchmarks for the described models. Strong scaling shows how fast a solution can be achieved if increasingly more resources are invested, whereas weak scaling shows how time to solution changes if resources are increased proportional to problem size, i.e., scale of the model. If the simulation performance is perfect, the time to solution should decrease proportionally to the amount of resources invested in strong scaling, and remains approximately the same in weak scaling, due to the distribution of workload. In this sense, in our study the strong scaling benchmarks measure the simulation time of a model while up-scaling the number of compute nodes, and the weak scaling benchmarks measure the simulation time while the model size is up-scaled proportionally to the number of compute nodes. The performance can thus be evaluated by the simulation time measured at different scales. In the weak scaling, in order to keep the same level of model activity, the cell number is scaled but the expected number of connections per cell is not, i.e., the expected number of primary (neuron-to-neuron) and third-factor (neuron-to-astrocyte and astrocyte-to-neuron) connections per cell is preserved.

Constructing the neuron-astrocyte model based on the experimental literature

This section describes the construction of the models based on the experimental literature. S3 Appendix contains additional details of the procedure and supplementary results.

Experimental data from the literature. We first collect experimental measures of spontaneous calcium activity in astrocytes [14, 45, 53–55] as well as neuronal spiking activity under several experimental conditions and in different brain regions [73, 74]. These experimental measures are compiled in S3 Appendix. They are used to fit some of the model parameters, and to guide selection of other parameters.

Fitting astrocyte parameters. Astrocyte parameters are selected by simulating Eqs (1) and (2) for 10^5 parameter sets and evaluating the resulting dynamics. Astrocyte dynamics are driven by Poisson inputs through IP_3Rs (through J_{syn} in Eq (2)). The 10^5 evaluated parameter sets differ in frequency of the Poisson events ($\lambda_{Poiss,A}$), the intensity with which they affect IP_3Rs (Δ_{IP_3}), the total calcium concentration in terms of the cytosolic volume (Ca_{tot}), the steady state value for IP_3 ($[IP_3]_0$), and the time constant that determines the speed of convergence towards the steady state (τ_{IP_3}).

These five parameters are randomly sampled from the predefined intervals (see S3 Appendix) while other parameters are kept constant at NEST default values. From the initial 10^5 parameter sets we select those models that exhibit calcium transients with the experimentally plausible period, duration, and peak values (see Table A in S3 Appendix). Finally, we test sensitivity by varying each optimized parameter in each model for $\pm 1\%$, $\pm 5\%$ and $\pm 10\%$ and testing if the results remain close to experimental when running the model for 5 different seeds of the random number generator. The selected parameter sets are described in Table C in S1 Appendix. To create an astrocyte population, five fitted parameters are randomly sampled from a Gaussian distribution. Mean, variance, and cutoff values of the Gaussian distribution are based on conclusions from sensitivity analysis.

Selecting neuron model parameters. Neurons are represented by AdEx model [63, 75] as implemented in NEST simulator. Excitatory and inhibitory neurons are respectively adapted from initial bursting and regular spiking neurons from Table 1 in [63]. The parameters are selected in such a way to ensure that the neurons respond to a SIC-mimicking current with a burst of spikes that fit the experimental data (details described in S3 Appendix; based on the SIC as illustrated in Fig 5 in [45]). The parameters of inhibitory neurons are further selected to produce a higher firing rate than the excitatory neurons, which is consistent with the literature (see Table B in S3 Appendix). Sensitivity to parameter change is tested by perturbing V_{reset} and b, two parameters that strongly affect spiking regime of AdEx neurons. To generate neuronal population, b and V_{reset} are drawn from Gaussian distribution with mean, variance, and cutoff values determined through sensitivity testing. The selected neuronal parameters are listed in Table C in S1 Appendix.

Selecting parameters of the neuronal network. We first select parameters that determine activity of the neuronal part only, the synaptic weights w_{exc}, w_{inh} and rates of Poisson inputs to neurons $\lambda_{\text{Poiss,E}}$, $\lambda_{\text{Poiss,I}}$. The selected parameters ensure low-frequency asynchronous activity regime for the neuronal part of the model such that spiking frequency of excitatory and inhibitory cells falls within the experimentally plausible range of values (see values from the literature compiled in Table B in S3 Appendix). The neuronal spiking rates are set to a lower end of the biologically plausible intervals to accommodate for the additional increase in the spiking rate due to SIC inputs. The following parameter values are used in all simulations $\lambda_{\text{Poiss,E}} = 2700$ spikes/s, $\lambda_{\text{Poiss,I}} = 2500$ spikes/s, $w_{\text{exc}} = 5$ nS, and $w_{\text{inh}} = -5$ nS. The Poisson rate is equal for all neurons of the same type, the synaptic weights are identical for all synapses of the same type.

Strength of neuron-astrocyte interactions, selection of $w_{\text{pre_to_astro}}$ and $w_{\text{astro_to_post}}$. We first determine the values for $w_{\text{pre_to_astro}}$ sufficient to induce astrocytic calcium transients in the absence of Poisson input to astrocytes ($\lambda_{\text{Poiss,A}} = 0$) and in the absence of astrocyte feedback to neurons ($w_{\text{astro_to_post}} = 0$). Similarly, we determine the values for $w_{\text{astro_to_post}}$ sufficient to induce SIC in the postsynaptic neurons in the absence of other (noise or synaptic) inputs. Next, we tune both parameters together to find the correct activity regime for each of the models shown in Results and S3 Appendix. In order to maintain dynamical regime of astrocytes in the presence of synaptic inputs, the rate of the astrocytic Poisson input is decreased to 70% of its value obtained from fitting single astrocytes.

Probability of interaction between a synapse and an astrocyte. In order to test synchronization in neuronal groups resulting from neuron-astrocyte interaction, it is crucial to control the number of postsynaptic neurons interacting with the same astrocyte, and the number of astrocytes sending SIC to the same neuron. In the `"block"` pool type this is determined by the numbers N_{A}, N_{E}, N_{I} and it is the same for each cell. Probability $p_{\text{third_if_primary}}$ decides the number of synaptic and SIC inputs per

astrocyte and neuron, respectively. In the `"random"` pool type, the number of postsynaptic neurons per astrocyte depends on $p_{\text{third_if_primary}}$ and differs between astrocytes (see Figs 1 and 2 in S3 Appendix). The number of astrocytes that send SIC to the same neuron has an upper limit defined by `pool_size`, but it is also determined by $p_{\text{third_if_primary}}$. Thus, for `pool_type = "block"` the choice of $p_{\text{third_if_primary}}$ is less important and we set it to be the same as the primary connection probability p_{primary} between pairs of neurons. However, in `pool_type = "random"` the selected values for $p_{\text{third_if_primary}}$ have to be much smaller in order to support both asynchronous activity and network bursting. Smaller probability of connection lead to less individual tripartite synapses created which has to be compensated by increase of $w_{\text{pre_to_astro}}$ and $w_{\text{astro_to_post}}$.

Hardware and software configurations for simulations

Simulations for the benchmarks are run with NEST 3.8 on 128-core compute nodes in the supercomputer JURECA at Jülich Research Centre. In each compute node, two MPI processes are used. In all benchmarks, nine simulations with three different seeds (three repeats each) for the random number generator are performed. Simulations for the model that reproduces experimental data are run with NEST 3.8 on a personal computer. Astrocyte parameter fitting to the values from the literature is performed using NEST 3.6 on 48-core compute notes in a computing cluster. All simulations are run with a computation time step of 0.1 ms biological time.

Data analysis

Mean neuronal firing rate. The mean neuronal firing rates of the network models used in this study are calculated with spike counts during the sampled window of the simulations:

$$f = \frac{\sum_{i=1..N} x_i}{N \cdot \Delta t} \tag{5}$$

where x_i is the spike count of neuron i during the sampled window, N is the number of neurons, and Δt is the duration of the sampled window.

Pairwise spike count correlation as a measure of synchrony. Pairwise spike count correlation is used as a measure of overall similarity of spike trains in two neurons, reflecting their underlying synchrony. For the benchmark and the model based on the experimental literature, the same approach is used for the calculation of correlation coefficient, i.e., Pearson's r, but different approaches are used for binning spikes due to different model activities. For the benchmark models (Fig 5), spike counts in 10-ms non-overlapping bins are obtained from $t = 1$ to $t = 11$ s of the simulation for all sampled neurons ($N = 100$), and pairwise spike count correlation is then calculated as:

$$r_{i,j} = \frac{\text{cov}(x_i(k), x_j(k))}{\sigma_{x_i(k)} \cdot \sigma_{x_j(k)}}, \tag{6}$$

where $x_i(k), x_j(k)$ are spike counts of the ith and jth sampled neurons in the kth bin. $\text{cov}(x_i(k), x_j(k))$ and $\sigma_{x_i(k)}$ and $\sigma_{x_j(k)}$ are the covariance and standard deviations of $x_i(k)$ and $x_j(k)$. The mean correlation $\overline{r}$ across all neuron pairs is then calculated as:

$$\overline{r} = \frac{2}{N(N-1)} \cdot \sum_{i=1..N-1} \sum_{j=i+1..N} r_{i,j}. \tag{7}$$

For the model based on experimental literature, spike trains of a neuron are binned using a sliding window of length 2 s which is shifted for 4 ms in each step. Binned spike

trains for two neurons, $x_i(t)$ and $x_j(t)$, are used to compute the correlation coefficient given by Eq (6). Distribution of correlation coefficients is shown in Fig 9-12D.

Single-neuron burst detection. To test the impact of neuron-astrocyte interaction through SIC, we evaluate single-neuron bursts arising from SIC inputs. We record burst onset, duration, frequency of bursts, and number of spikes per burst in each neuron. Burst onsets are used to evaluate SIC-induced synchronization in pairs of neurons, the results are reported in Fig 9-12D. For each neuron, the properties of bursts are quantified as follows:

1. Find $t_{\text{sic}-\text{on}}$, $t_{\text{sic}-\text{off}}$, onset and offset times for all SIC inputs to the considered neuron (regardless of the sending astrocyte).

2. Find the number of spikes within the interval $[t_{\text{sic}-\text{on}}, t_{\text{sic}-\text{off}} + \texttt{max_after_sic}]$; spiking should not start before SIC but it may continue for a short time after SIC determined by parameter `max_after_sic`.

3. The spikes have to be close enough to each other to belong to the same burst. Closeness is determined by the parameters `max_allowed_distance_exc` and `max_allowed_distance_inh` for the two neuron types. Here, these two parameters are set to 2 s and 400 ms, which is shorter than the average inter-spike-interval in these neuron types.

4. Burst onset is the time of the first spike. Burst duration is the time between the last and the first spike in the burst. Burst frequency is calculated as the total number of bursts divided by the total simulation time.

Detection of astrocyte transients. Frequency and duration of calcium transients shown in Figs 9-12A are determined from the calcium recordings in each astrocyte as follows:

1. Threshold the calcium recording using the same threshold for triggering SIC ($\theta_{\text{SIC}} + 1$ nM).

2. Noisy inputs to astrocytes cause calcium to flicker around the threshold which results in spurious threshold crossings. Multiple crossings are merged if they are too close, i.e. if they are closer than the parameter `max_allowed_distance_astro`. Fixing this parameter to 2 s gives good results for the network activity regimes considered in this study.

3. Transient onsets are ascending crossing points found above, while transient endings are descending crossing points. Duration of calcium transients is calculated as the time between ending points and onsets.

4. Frequency of astrocytic calcium transients is computed as the total number of transients recorded during the simulation time divided by the simulation time.

Distance of burst onsets as a measure of synchrony. Synchrony in pairs of spiking neurons is evaluated as a distance between their burst onsets in successive SIC-induced bursts. The metric is inspired by synchrony detection adopted in [45], and it also reflects phase synchrony in coupled spiking neurons. The metric is implemented as Python function and supplied with the rest of the code.

Results

Benchmark results confirm efficiency of the implemented NEST support for astrocytes

In order to evaluate the performance of the implemented models and functions, we run benchmarks with neuron-astrocyte network models as described in Methods. Following the previous approach [72], we use NEST and beNNch to measure the time spent on network creation, network connection, and state propagation. The state propagation consists of multiple phases, labeled as follows. "update" is for advancing the dynamical states in each cell and device. "spike CCD" and "SIC GD" are the processes necessary for the exchange of information in parallel computing: "spike CCD" is the collocation, communication, and delivery of spikes, and "SIC GD" is the gathering and delivery of the SIC events. "other" stands for the part of time that cannot be attributed to the three phases above.

Fig 6 shows the first set of benchmark results. In the strong scaling benchmarks, the network connection time reaches a minimum for three nodes and then increases, while the state propagation time always decreases with the scale. In the weak scaling benchmarks, both network connection time and state propagation time increase with the scale, except the "update" phase which advances the dynamical states in individual cells and hence can be highly parallelized. The network creation time also reflects parallelized workload and is relatively unaffected by strong or weak scaling, or the model used. All models spend less than 1 s on network construction (creation + connection), and the real-time factor (wall-clock time spent on simulation/biological time of the model) for state propagation is always less than three.

Consistent with Fig 5, the "synchronous" model always produces many more spikes than the "sparse" model. Nevertheless, this only slightly affects the simulation time. The mean neuronal firing rate of the "synchronous" model is more than twice that of the "sparse" model (4.76 versus 11.95 spikes/s for 20,000 cells; mean of nine simulations). However, in both strong and weak scaling benchmarks, the state propagation times are similar, with a difference of 7.0% to 8.6% compared to the "sparse" model (Fig 6). This limited effect of higher firing rate on state propagation time reflects the small differences in each of the phases (Fig 6). This shows a good efficiency in the communication and processing of spikes between and within the cells, and the fact that `sic_connection`s send continuous SIC signals regardless of the level of model activity.

The "surrogate" model has a similar mean neuronal firing rate as the "sparse" model (4.64 versus 4.76 spikes/s for 20,000 cells) but spends less time on state propagation, which is mainly due to the shorter "update" phase (Fig 6). Since `astrocyte_surrogate` does not have astrocytic dynamics and sends predefined SICs instead, in the "surrogate" model the time spent on the "update" phase is mostly for the update of states in the neurons. The "sparse" model spends 80.9% to 112.1% more time on "update", compared to the "surrogate" model (Fig 6). This approximately represents the additional computational demands in the "update" phase due to the astrocytic dynamics. On the other hand, since the connectivity function does not distinguish `astrocyte_lr_1994` and `astrocyte_surrogate`, the network creation and connection time of the "surrogate" model are similar to the "sparse" model.

The benchmark results with four primary (neuron-to-neuron) connectivity rules are shown in Fig 7. The four models have a similar performance in all aspects, except that the fixed out-degree rule shows a longer network connection time than the other three because it cannot be parallelized. Note that the data of the "Bernoulli" model is the same as the "sparse" model in Fig 6, where the pairwise Bernoulli rule is used for the primary connections, and the other three models have the same expected numbers of primary and third-factor connections as the "Bernoulli" model.

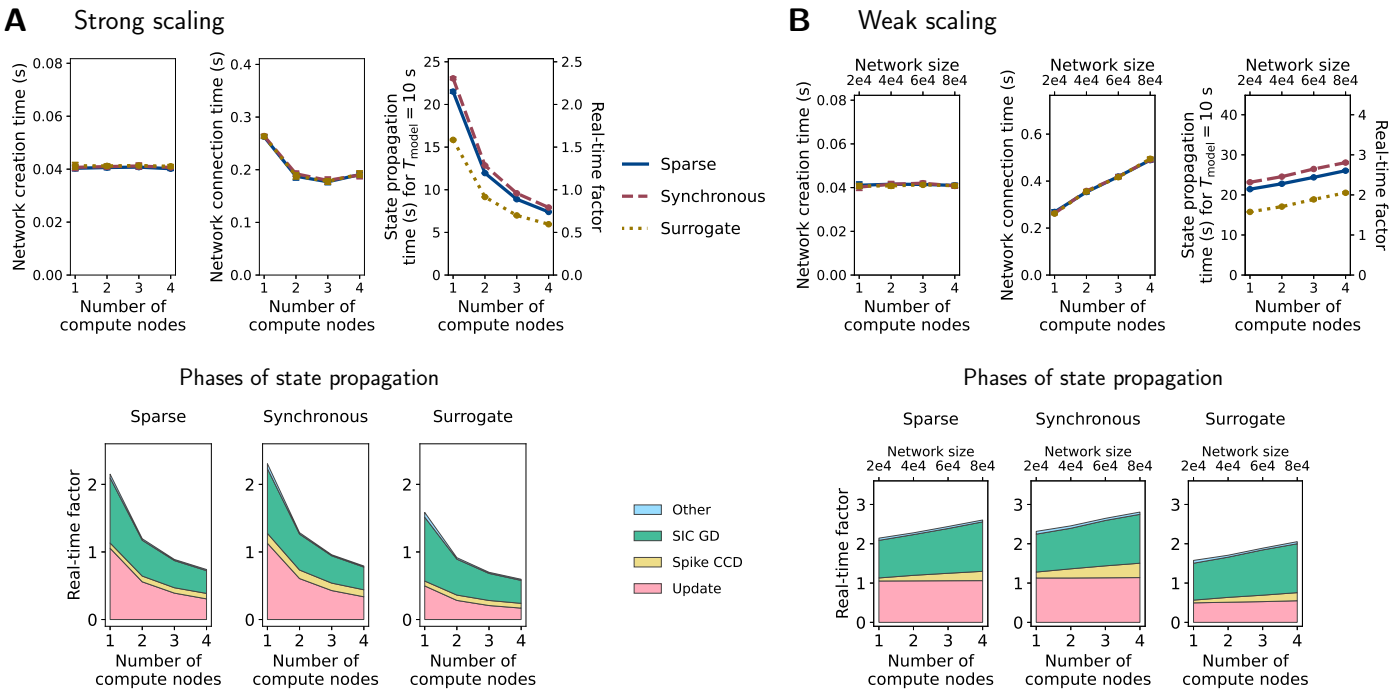

Fig 6. Benchmarks with neuron-astrocyte network models. (A) Strong scaling. In this type of benchmark, the network size stays constant (20,000 cells), but the number of compute nodes used is scaled. (B) Weak scaling. In this type of benchmark, the model size and the number of compute nodes are scaled together. The first row in (A) and (B) shows network creation time, network connection time, and state propagation time for $T_{\mathrm{model}} = 10$ s (biological time of the model) and its real-time factor (wall-clock time spent on simulation/T_{model}). Error bars indicate standard deviations across nine simulations. In some cases the error bar is very small and hence not visible. The second row shows the phases of state propagation in terms of average real-time factor. "update": advancing the dynamical states in each cell and device. "spike CCD": collocation, communication, and delivery of spikes. "SIC GD": gathering and delivery of SIC events. "other": the part of time that cannot be attributed to the three phases above. "sparse", "synchronous": models with sparse and synchronous activities, respectively. "surrogate": Model using `astrocyte_surrogate` (no astrocytic dynamics). For specifications of these models, see Tables A and B in S1 Appendix. For the dynamics of the "sparse" and "synchronous" models, see Fig 5.

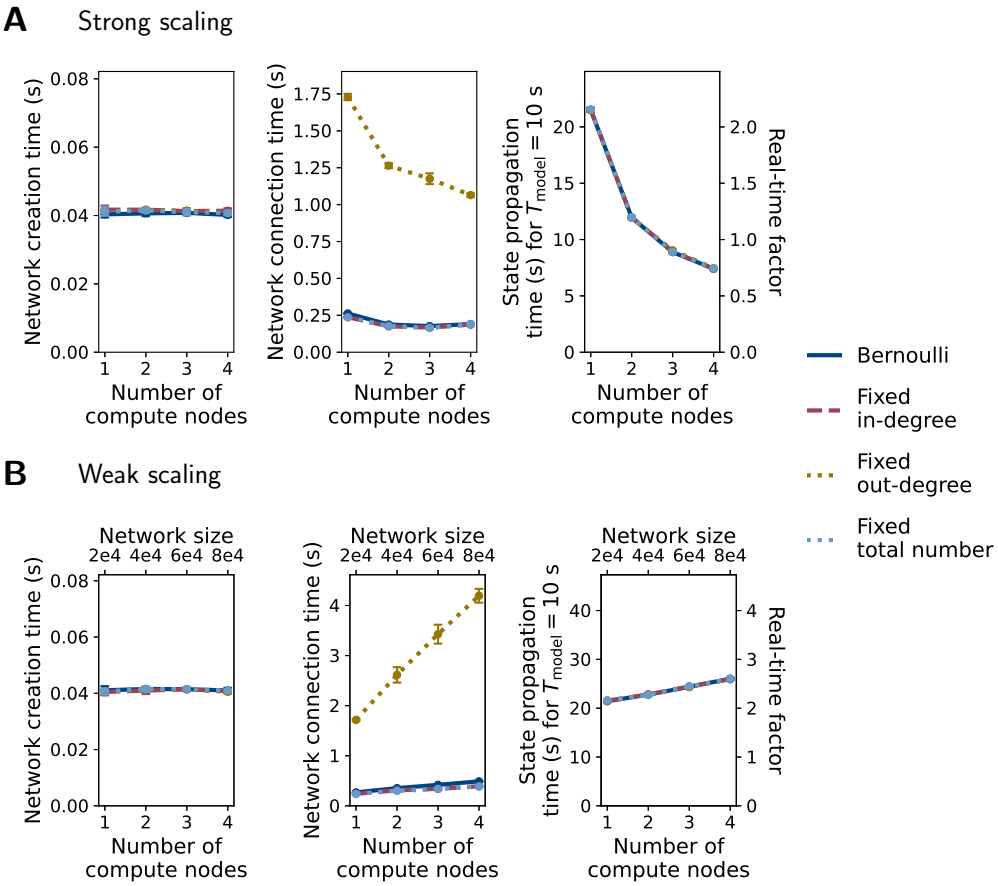

Fig 7. Benchmarks with different primary (neuron-to-neuron) connectivity rules. (A) Strong scaling. The network size is 20,000 cells. (B) Weak scaling. The four tested connectivity rules are pairwise Bernoulli, fixed in-degree, fixed out-degree, and fixed total number. For specifications of these rules, see [64]. Model parameters other than the connectivity rule are the same as the "sparse" model in Fig 6. Notations and benchmark configurations are the same as in Fig 6.

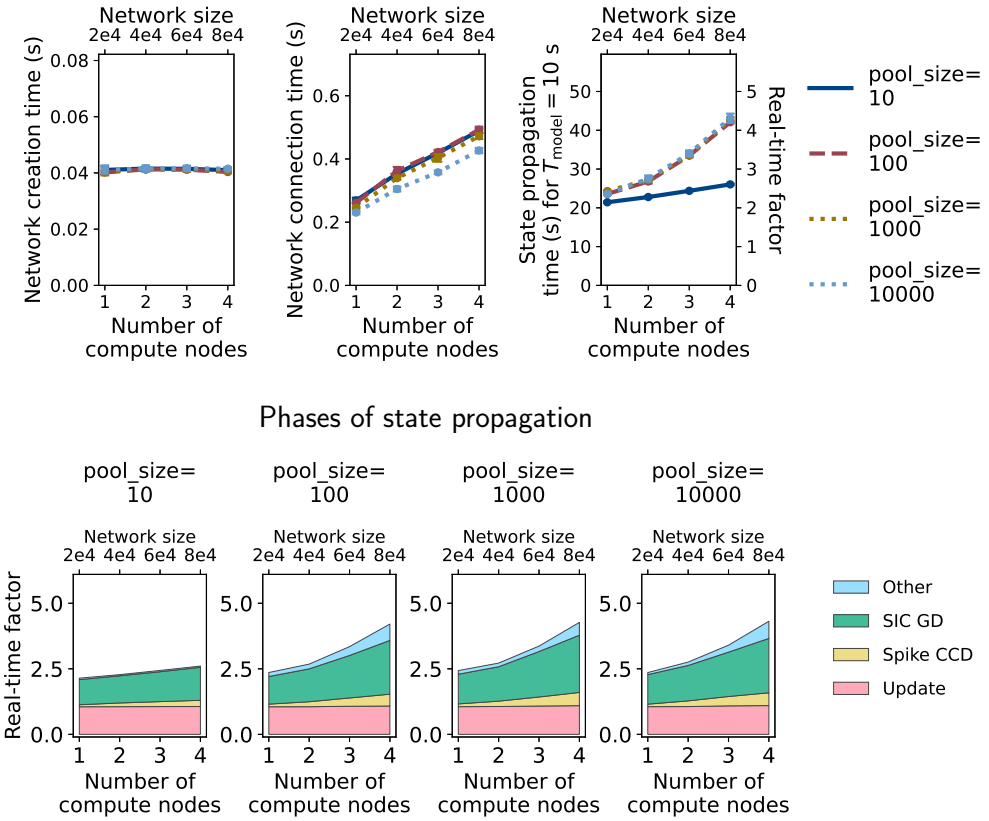

Fig 8. Weak scaling benchmarks with different astrocyte pool sizes. Weak scaling benchmark results with astrocyte pool sizes per neuron (`pool_size`) from 10 to 10,000. Model parameters other than `pool_size` are the same as the "sparse" model in Fig 6 and the "Bernoulli" model in Fig 7. Notations and benchmark configurations are the same as in Figs 6 and 7.

Weak scaling benchmark results for different astrocyte pool sizes are shown in Fig 8. While network connection time is only mildly affected by pool size, pool sizes of 100 and larger lead to increased state propagation times compared to pool size 10. For four nodes and a pool size of 100, the increase is 61.5%, for a pool size of 10,000 it is 65.6%. This increase is driven by increased spike and SIC communication times as well as an increased "other" time (Fig 8, second row). This difference in scaling behavior appears to be due to different communication requirements. If the astrocyte pool size is well below the average number of incoming astrocytic connections per target neuron (astrocytic in-degree, 400 in our models), the number of target neurons to which any astrocyte connects is close to the pool size; for large pools, on the other hand, it is determined by the astrocytic in-degree. In particular, for a pool size of 10, each astrocyte connects to 10 target neurons on average. In this case and when using four compute nodes with eight MPI processes in total, I_{SIC} needs to be transmitted to all MPI processes only for fewer than 10% of all astrocytes. For a pool size of 100 and larger, on the other hand, I_{SIC} from all astrocytes must be communicated to all MPI processes, requiring higher bandwidths. The data for a pool size of 10 are the same as the "sparse" model in Fig 6.

Use case: Astrocytes promote neuronal synchronization *in silico* through neuron-astrocyte interaction

In this use case, we demonstrate how the developed NEST support for astrocytes can complement a selected experimental study described in [45, 47]. By recording from rat cortical, hippocampal, and thalamic slices, the authors of [45, 47] provided evidence for synaptic glutamate release, astrocyte activation, SIC generation mediated by extrasynaptic NMDARs, and subsequent slow calcium responses (SCRs) in neurons. They demonstrate that SICs induce synchrony in groups of neurons and hypothesize that this synchronization results from neuron-astrocyte interactions. The NEST support for astrocytes implements the above experimental observations at the level of details compatible with the spiking network formalism. In what follows, we explore synchrony in the computational model of neuron-astrocyte network.

First, we reproduce the duration and frequency of spontaneous calcium transients in astrocytes reported in experimental studies. The frequency of SIC occurrences (and calcium transients that induce it) is estimated to be 1.26 ± 0.2 SIC/min in the slices pre-exposed to glutamate and 0.07 ± 0.01 SIC/min in control [45]. Other studies, that examine calcium dynamics in astrocytes but do not consider SIC, report frequency of calcium transients to be 1.2 transients/min [53], 4 transients/min [55], and 0.5 transients/min [54]. Duration of calcium transients is found to be between 1–20 s [55] and 9–18 s [54]. These values collected from experimental studies are systematically listed in S3 Appendix. We fit a model of an isolated astrocyte, and specifically the parameters $\mathrm{Ca}_{\mathrm{tot}}$, $[\mathrm{IP}_3]_0$, Δ_{IP_3}, and τ_{IP_3} as well as the rate of the input Poisson noise $\lambda_{\mathrm{Poiss,A}}$ to reproduce these values (see Methods and S3 Appendix). All model parameters are listed in Table C in S1 Appendix and also in a JSON file supplied with the code for model implementation. The obtained model generates transients with frequency of about 0.5–1.5 per minute and duration of between 1–5 s as shown in Fig 9A.

Next, we focus on the experiment from [45] in which extracellular glutamate was increased through pre-exposure to glutamate while neuronal spiking was pharmacologically blocked by TTX. We construct a population of $N_{\mathrm{A}} = 100$ astrocytes, $N_{\mathrm{E}} = 400$ excitatory, and $N_{\mathrm{I}} = 100$ inhibitory neurons. Astrocytes have only Poisson input mimicking the processing of extracellular glutamate, while neurons receive weak Gaussian noise and cannot spike without SIC input from astrocytes to the postsynaptic neuron. In response to a SIC input, neurons develop a short burst containing normally 2–4 (but up to 14) spikes and lasting for about 1 s. In this model system, this burst is interpreted as a correlate of a slow calcium response measured in [45], rather than a sequence of spikes (which cannot occur in experiments with slices exposed to TTX). Neurons are randomly connected with probability $p_{\mathrm{primary}} = 0.2$, however the synaptic weights are set to zero to account for the blocking of spiking via TTX. The setting `pool_type = "block"` with `pool_size = 1` structures the neuron-astrocyte interaction. This choice of parameters results in 100 non-overlapping neuronal groups, each consisting of 4 excitatory and 1 inhibitory neuron that can receive SIC from the same astrocyte. A neuron can receive SIC from only one astrocyte. Fig 9C illustrates calcium activity of a single astrocyte (middle sub-panel) induced by Poisson input. Activity of presynaptic neurons is shown as rasterplot (top sub-panel). However due to synaptic weights set to 0, this activity does not affect astrocyte. Synchronization induced by SIC input between an astrocyte and five neurons interacting with this astrocyte is illustrated in the bottom of Fig 9C. Fig 9D demonstrates increased synchrony in groups of neurons connected to the same astrocyte compared to the overall level of synchronization between neurons in the model. Synchrony is evaluated in two ways, either as a distance between onset of successive single-neuron bursts in pairs of neurons (upper panel) or as pairwise correlation (lower panel), for details see Methods.

Bursts are well aligned in neurons that interact with the same astrocyte (distribution is collapsed to values very close to zero). Correlation coefficients are very small in general due to sparse activity in the model. In both cases, synchronization evaluated between neurons that receive inputs from the same astrocyte is significantly higher compared to synchronization evaluated across all pairs of neurons in the model (Kolmogorov-Smirnov test, $p_{\text{val}} = 2.85e^{-42}$ for comparison of burst onset times, $p_{\text{val}} = 3.07e^{-112}$ for comparison of pairwise correlations; values after Bonferroni correction done for all tests in this section and all related tests in S3 Appendix).

The same result is reproduced in a model with spiking neurons and nonzero synaptic weights (Fig 10). The network has low-frequency asynchronous activity, where excitatory neurons spike at frequency of about 0.1 spikes/s while inhibitory neurons spike at frequency of about 2 spikes/s. Single-cell bursts resulting from SIC inputs are visible in the rasterplots of (sparser) excitatory activity in Fig 10B. Same as before, Fig 10C illustrates synchronization between an astrocyte and its postsynaptic neurons at each astrocytic calcium transient. The presynaptic activity, shown by the top sub-panel, contributes to astrocyte inputs in this case. Fig 10D shows increased synchronization (both measured as distance between burst onsets, and as pairwise correlation) between neurons connected to the same astrocyte (Kolmogorov-Smirnov, $p_{\text{val}} = 0$ for burst onset times, and $1.48e^{-171}$ for pairwise correlation; values after Bonferroni correction). Reproducibility of this result is confirmed by running the same simulation for different seed of the random number generator and obtaining similar results (see Fig 3 in S3 Appendix).

Increasing the overall input to an astrocyte by increasing the weight $w_{\text{pre_to_astro}}$ from 0.2 to 0.31 results in emergence of network-wide bursts lasting on average 5 s, as shown in Fig 11. Although the global synchronization increases in this activity regime, synchronization between neurons interacting with the same astrocyte still exceeds synchronization computed for all pairs of neurons in the model (Kolmogorov-Smirnov test, $p_{\text{val}} = 0$ for burst onset times, $8.92e^{-247}$ for pairwise correlation; values after Bonferroni correction).

So far, neurons form well separated groups, each group receiving inputs from only one astrocyte. The experimental study inspiring this model [45] shows that neurons can belong to more than one synchronized group and hypothesizes that structure of neuron-astrocyte interactions might create such groups. The NEST support for astrocytes implements random connectivity scheme (`pool_type = "random"`, see Fig 2) in which both many-to-one and one-to-many connectivities can occur in astrocyte-neuron connectivity and, in addition, an astrocyte can interact with any neuron in a network rather than with a dedicated group of neurons. We construct a network model using this connectivity schema and evaluate model dynamics as shown in Fig 12. The maximal number of astrocytes is determined by the model parameter `pool_size`, which is set to 5 here. The connectivity depends on two probabilities, the probability to establish a neuron-neuron synapse, p_{primary} set to 0.2 here, and a probability to connect that synapse with an astrocyte, $p_{\text{third_if_primary}}$ set to 0.03 here (but see the same result reproduced with a bigger probability value, $p_{\text{third_if_primary}} = 0.05$, in Fig 4 in S3 Appendix). The exact number of neuron and astrocyte inputs in this model is shown in Fig 2 in S3 Appendix. Due to overlap of astrocytic domains, synchronization within neuronal groups is established faster and it is easier to reach global bursting regime. Still, asynchronous low-frequency spiking regime is achievable also in this model, and the synchronization between neurons receiving SIC from the same astrocyte remains higher than the overall synchronization in the neuronal network (Kolmogorov-Smirnov, $p_{\text{val}} = 0$ for comparison of burst onsets, 0 for comparison of pairwise correlations; values after Bonferroni correction). Increased synchronization between neurons interacting with the same astrocyte holds in the model

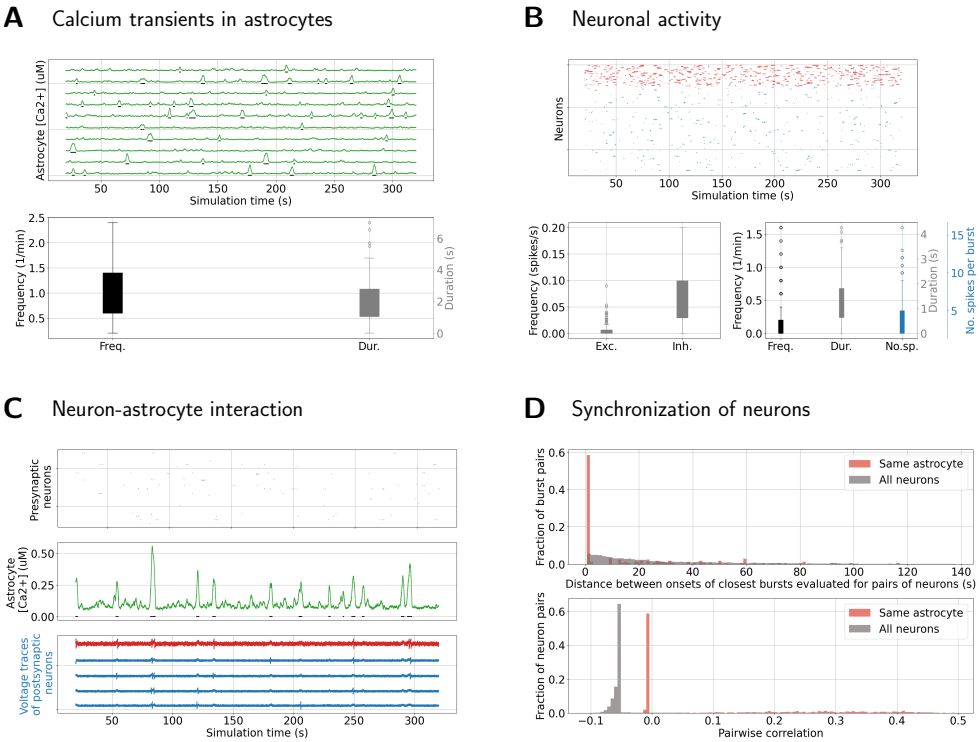

Fig 9. Reproducing experiment with TTX blocking - neurons do not spike without SIC input and all synaptic weights are set to zero except $w_{\text{astro_to_post}}$. (A) Spontaneous calcium transients in ten random astrocytes (top sub-panel). Frequency and duration of calcium transients (bottom sub-panel) corresponds to experimental values from the literature. (B) In this model, neuronal spiking exists only within single-neuron bursts, the neuronal response to SIC inputs (top panel). Blue dots depict activity of excitatory neurons and red of inhibitory neurons. Neuronal firing is sparse in this model (bottom left sub-panel). Frequency, duration, and number of spikes per single-neuron burst is shown in the bottom right sub-panel. (C) Single astrocyte (middle panel) is depicted together with its 5 postsynaptic neurons (bottom panel, blue voltage traces - excitatory neurons, red traces - inhibitory neurons) and all of its (excitatory) presynaptic neurons (top panel). Synchronization induced by calcium transients and resulting SIC can be seen in voltage traces of postsynaptic neurons. (D) Neuronal synchrony is evaluated as a difference in onsets of successive burst events (top panel) and as the pairwise correlation between binned spike trains (bottom panel). Neurons interacting with the same astrocyte develop synchrony that exceeds synchrony level computed from the entire population (Kolmogorov-Smirnov test, $p_{\text{val}} = 2.85e^{-42}$ for comparison of burst onset times in upper panel, $p_{\text{val}} = 3.07e^{-112}$ for comparison of correlation coefficients in lower panel; values after Bonferroni correction).

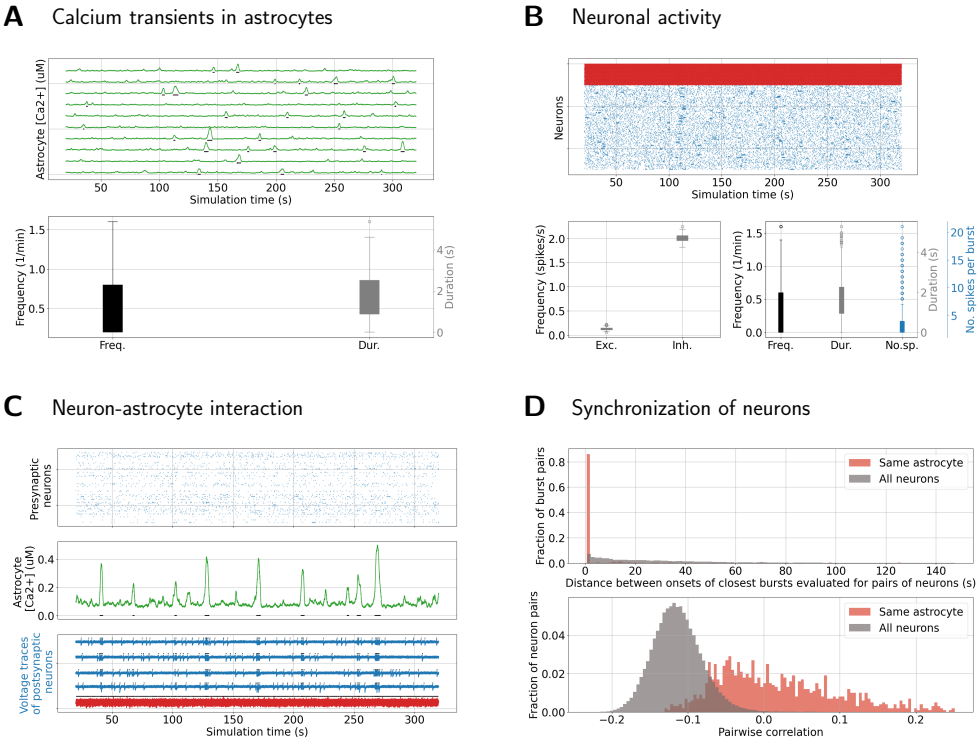

Fig 10. Synchronization in neuron-astrocyte networks with `pool_type = "block"` connectivity and asynchronous activity regime. (A) Spontaneous calcium transients in ten random astrocytes (top sub-panel). Frequency and duration of calcium transients is shown in the bottom sub-panel. (B) Rasterplot shows network activity, blue dots correspond to spiking in excitatory neurons, red dots in inhibitory neurons (top panel). Neurons show asynchronous spiking with frequency of 0.1 spikes/s for excitatory and 2 spikes/s for inhibitory neurons (bottom left panel). Single-cell bursts are visible in the rasterplots. Distributions of single-cell burst frequency, duration, and number of spikes per burst across all neurons in the model are shown in the bottom right sub-panel. (C) Single astrocyte (middle panel) with its five postsynaptic neurons (bottom panel) and all presynaptic neurons (rasterplot, top panel). (D) Both measures of synchrony, onset of successive bursts in pairs of neurons and pairwise correlation, show increased synchrony in neurons that receive SIC inputs from the same astrocyte (Kolmovorov-Smirnov test, $p_{\text{val}} = 0$ for comparison of burst onset times, $p_{\text{val}} = 1.48e^{-171}$ for comparison of correlation coefficients; values after Bonferroni correction).

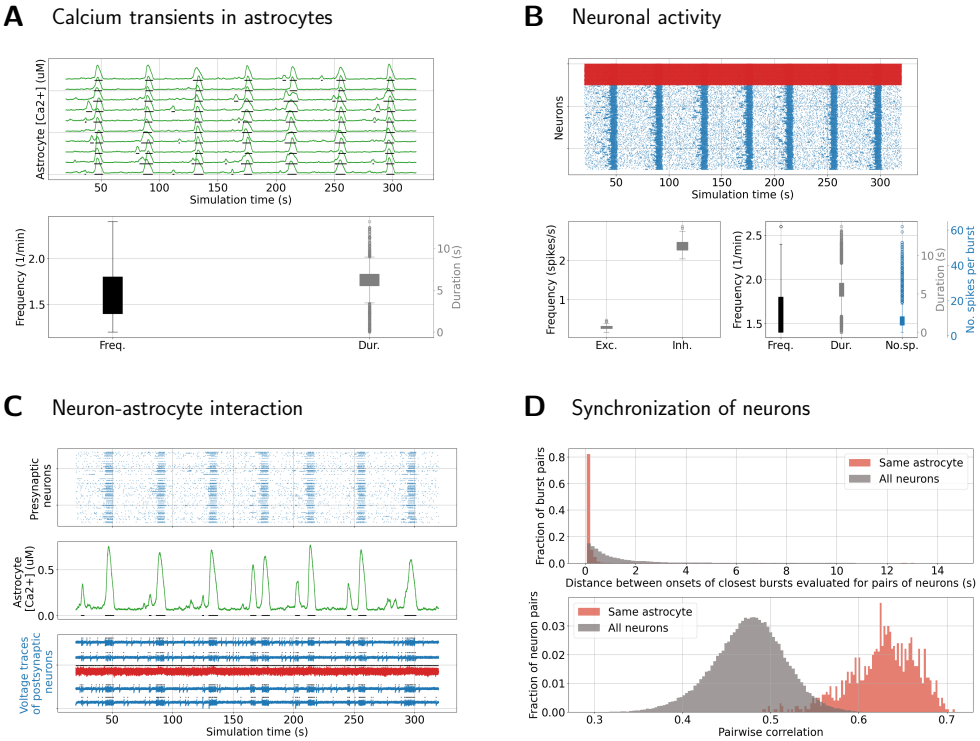

Fig 11. Synchronization in neuron-astrocyte networks with `pool_type = "block"` and global network bursting activity. (A) Astrocytic calcium transients synchronize in this case, as shown in the top panel. Frequency and duration of calcium transients also increase compared to the asynchronous activity regime, as shown in the bottom sub-panel. (B) Rasterplots (blue-excitatory neuron spiking, red-inhibitory neuron spiking) show global network bursts appearing each 50–100 s (top panel). As a result of increased overall activity, spiking frequency increases in both excitatory and inhibitory neurons (bottom left) as well as the frequency, duration, and number of spikes per single-neuron bursts (bottom right). (C) Single astrocyte (middle panel), its five postsynaptic neurons (bottom panel) and its presynaptic neurons (top panel) all follow global synchronous activity. (D) Although the global network synchrony is present in this model, the neurons that interact with the same astrocytes still show significantly higher level of synchrony compared to average neurons (Kolmogorov-Smirnov test, $p_{\text{val}} = 0$ for comparison of burst onset times, $p_{\text{val}} = 8.92e^{-247}$ for comparison of correlation coefficients; values after Bonferroni correction).

with `pool_type = "random"` that exhibits network bursting regime, as shown in Fig 6 in S3 Appendix. Similarly as before, network bursting regime is achieved by increasing the amount of glutamatergic inputs to astrocytes, i.e. by increasing the weight coefficient $w_{\text{pre_to_astro}}$ from 1 to 1.5.

In order to support the here presented results, we provide several additional tests in S3 Appendix. The simulations shown in Fig 10 (`pool_type = "block"`, asynchronous network activity) and in Fig 6 from S3 Appendix (`pool_type = "random"`, network bursting) are repeated for a synaptic delay ten times smaller (`"delay"` parameter is decreased from the NEST default value of 1 ms to 0.1 ms). Synaptic delay impacts the speed of neuron-neuron and neuron-astrocyte exchange and can affect the global activity regime. The simulations confirm robustness of our results against change in synaptic delay. We also verified that results presented here indeed show the steady state of the system. The simulations in Fig 10 and in Fig 6 from S3 Appendix are repeated for much longer simulation time. The models are first simulated for 15 min, and then for additional 5 min (as opposed to 20 s and 5 min used in other figures). Analysis is done for the last 5 min of simulations and the results confirm previous findings.

In summary, we show the emergence of synchronization in small groups of neurons as a result of SIC inputs arriving from the shared astrocyte partner. Our *in silico* results support the findings and test hypotheses set in [45, 47]. Furthermore, the results suggest important role of astrocytes in shaping the global neural activity states through local neuron-astrocyte interactions.

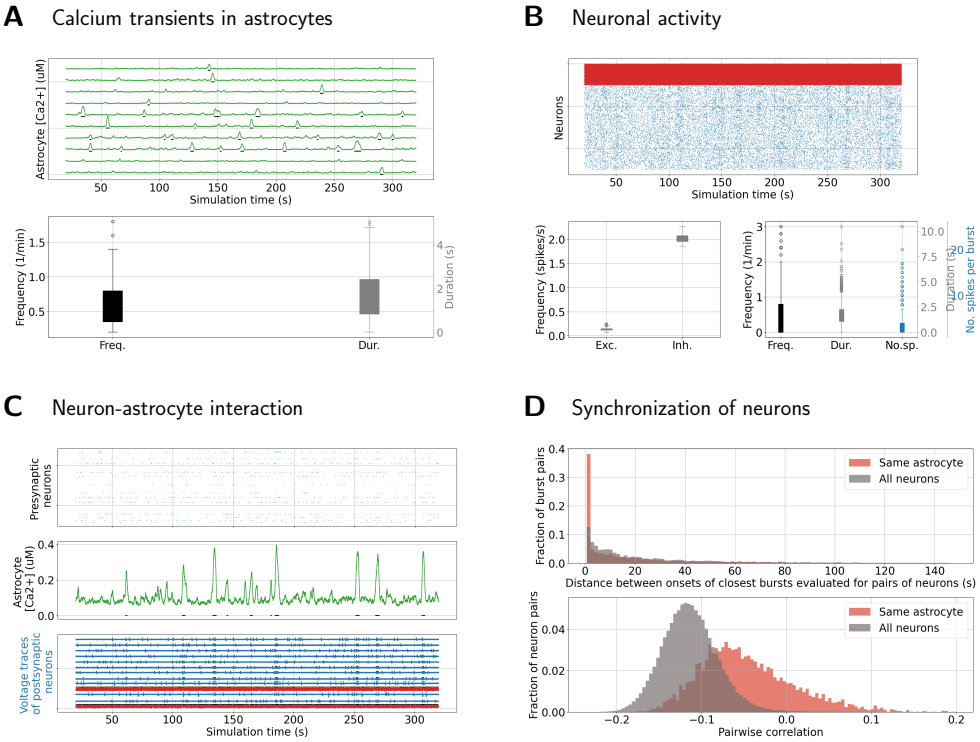

Fig 12. Synchronization in neuron-astrocyte networks with `pool_type = "random"` and global low-frequency asynchronous activity. (A) Astrocytic calcium transients in ten random astrocytes (top), frequency and duration of these transients (bottom). (B) Neurons show asynchronous spiking with similar frequencies as in Fig 10. Frequency, duration and number of spikes per single-neuron burst are also similar to those in Fig 10. Single-neuron bursts are less visible in the rasterplot (top; blue - spikes in excitatory neurons, red - in inhibitory neurons) and instead larger synchronous groups could be seen occasionally. (C) Single astrocyte (middle) with its presynaptic neuronal inputs (rasterplot, top) and its postsynaptic neurons (voltage traces, bottom). This connectivity type allows more output neurons per astrocyte and bigger variability in number and type (excitatory vs inhibitory) of neurons per astrocyte compared to the block-type connectivity. Astrocyte-driven synchrony in the postsynaptic neurons is still visible. (D) Although neurons can receive inputs from multiple astrocytes and potentially participate in multiple synchronous groups, synchronization between neurons interacting with the same astrocyte is still significantly higher than synchronization evaluated across all neurons in the network (Kolmogorov-Smirnov, $p_{\text{val}} = 0$ for comparison of burst onset times, $p_{\text{val}} = 0$ for comparison of correlation coefficients; values after Bonferroni correction).

Discussion

We develop a new solution for incorporating glial cells, their dynamics, and their interaction with neuronal cells into an established formalism for modeling neural systems. As a reference, the solution is fully integrated into the NEST simulation code, a popular, community developed, open-access tool for modeling large-scale spiking neuronal networks, and through NEST into the EBRAINS infrastructure for computational modeling and data analysis in neuroscience. Throughout the article, we list details of this reference implementation of our concepts, confirm efficiency of the implementation through a series of benchmarks, and finally utilize the tool to reproduce and expand the selected experimentally shown result, namely how astrocytes support synchronization in groups of neurons. The presented tool supports reproducible and collaborative large-scale modeling of neuron-astrocyte circuits and answers to the increasing interest in these models in the computational neuroscience community [32].

The technology described here lays the foundation for a comprehensive and efficient modeling and simulation platform for neural systems composed of both neuronal and non-neuronal cells. The first step requires developing a method to define tripartite interactions in cellular populations of arbitrary size. For this we present the `TripartiteConnect()` concept, that allows to simultaneously represent the pre- and post-element of a synapse and the respective interaction with an astrocyte. With this concept all connectivity rules (apart from those depending on explicitly defined spatial organization) defined in [64] can now include interaction with a third factor like astrocytes. In the present work the arguments of `TripartiteConnect()` are neuronal and astrocyte populations specified using particular neuron and astrocyte models. For astrocytes, we describe a well-known Li-Rinzel model of calcium dynamics [41], based on an earlier model for IP_3 kinetics and calcium exchange between ER and cytosol [40]. For neurons, we extend the AdEx spiking neuron model [62, 63, 75], by currents induced by astrocyte activity. The dynamics of neuron-astrocyte interactions also follow a model from the literature, first proposed in [42] and later frequently used in a number of computational studies [32]. The impact of neurons on astrocytes accounts for astrocytic mechanisms depending on synaptically released glutamate, while the impact of astrocytes on neurons depends on the mechanism of slow inward currents (SICs) [42, 45].

The technology for simulating continuously coupled equations in a distributed computing setting as required for large-scale neuronal systems is available [76]. This enables, for example, the inclusion of gap junctions in a network model. However, due to our phenomenological description of the SIC mechanism, the full waveform relaxation framework is not required. The assumption of a finite delay in the interaction enables the use of the same optimization as for the spiking interaction: communication is only required in intervals of the minimal delay in the system [69]. A code based on the molecular mechanisms of systems biology can unify the interaction types including spikes, gap junctions, and SIC currents, but for the price of higher computational costs.

The astrocyte and neuron models of the present study reflect common choices across the literature [29, 32], and also correspond to the models that are available in common simulation tools [37, 39, 77]. As such, our choice caters for the needs of the community and facilitates model development across existing tools. We further support this goal by providing a systematic comparison of models, their variable and parameter names used in the literature, in this article, and in the user-level documentation of our reference implementation (see S2 Appendix). Reproducibility and model development are additionally facilitated by a systematic description of model dynamics and model parameters in a tabular format in S1 Appendix. This format, first proposed in [61] standardizes neuronal network description and supports reproducible and reusable model development. We adapt the format originally developed for neuronal networks to include astrocytes and neuron-astrocyte interactions. We believe that this formalism

should become standard for systematic and rigorous description of neuron-astrocyte models in the literature.

While here we opt for well-known models from the literature for demonstration, the framework for astrocyte modeling extends to other experimentally confirmed mechanisms including more complex models for astrocytic calcium dynamics, neuron-astrocyte interaction through other neurotransmitters (GABA), release of other molecules including D-serine and ATP, and further mechanisms. In this study, we consider only the basic AdEx neuron model as, for example, available in the NEST simulation code, but other point neuron models can be similarly generalized to receive astrocyte inputs. Connecting cells according to their explicitly specified spatial location is another potential future development that would benefit from more comprehensive morphometric data and future neuroanatomical studies. The NEST simulation code already provides a framework for spatially organized connectivity.

Benchmarking the technology

The benchmark results demonstrate the efficiency of our reference implementation when using parallel computing resources. The strong scaling benchmark examines the simulation performance with fixed model size and up-scaled computing resources. Parallelization decreases network connection time and state propagation time. The weak scaling benchmark examines the performance with coupled up-scaling of model size and computing resources. In the weak scaling the time spent for phases of the simulation that require communications between parallel processes (e.g., network connection, "spike CCD", "SIC GD") increases with the scale. Nevertheless, both strong and weak scaling benchmarks show a good performance in network construction time and state propagation time. With one compute node, the real-time factor for state propagation is close to two in all tested benchmark models. The real-time factor is further reduced by strong scaling, and in weak scaling it remains below three for most of the tested benchmark models (Figs 6, 7) and below five in benchmarks with large astrocyte pool size (8).

In the first set of benchmarks, three models are used to evaluate how overall model activity and astrocytic dynamics affect simulation performance (Fig 6). Parameters of the "sparse" and "synchronous" models are chosen to yield sparse and synchronous neuronal activity, respectively. Even though the difference in neuronal activity is large, the overall simulation times of the "sparse" and "synchronous" models are similar, suggesting that the performance is only slightly affected by the level of activity in the tested models. In the "surrogate" model, the astrocytes are replaced by surrogate cells which do not have astrocytic dynamics but send predefined SIC currents to their target neurons. The comparison between the "sparse" and "surrogate" model exposes the additional amount of time spent on astrocytic dynamics. The result suggests that, in a network model where the number of astrocytes equals the number of neurons, the astrocytes are equally expensive as the neurons (Fig 6).

The second set of benchmarks shows that models with different primary (neuron-to-neuron) connectivity rules have very similar performance in general, except for the non-parallelizable fixed out-degree rule (Fig 7). The third set of benchmarks shows the effects of astrocyte pool size per neuron, i.e., the number of astrocytes that each neuron can receive inputs from. The benchmark data suggest that large astrocyte pool size increases the workload in communications for spikes and SIC currents (Fig 8).

Overall, the benchmark results show good scaling performance and limited effects of model activity or network-level parameters on the performance. This suggests that our technology is capable of simulating diverse large-scale neuron-astrocyte network models.

Use case for the technology

As a use case, we reproduce and extend the selected experimental findings [45] by implementing, fitting to the available data from the literature, and simulating a set of computational models of neuron-astrocyte networks. The study by Pirttimaki et al. [45] focuses on the biophysical origin of SIC current and its impact on neuronal activity. The phenomenon is observed in spontaneously active circuits and in circuits where spontaneous activity is enhanced by extracellular glutamate. The study demonstrates how astrocytes support synchronization in neuronal groups, possibly in neurons interacting with the same astrocyte, in cortical, hippocampal, and thalamic slices [47, 52]. We construct a computational model that closely approximates the experimental setup of [45], conduct equivalent *in silico* experiments, and demonstrate that astrocytes promote synchronization in neuronal groups across various connectivity schemes and under different global activity regimes.

In order to reproduce realistic spontaneous activity in astrocytes, we conduct an extensive survey of experimental evidence in the literature, summarized in S3 Appendix, and fit a single astrocyte model. Spontaneous calcium activity has been observed (using confocal microscopes) in astrocytes in hippocampal slices, in soma, processes, and microdomain areas in wild type mice [53]. Typical spontaneous calcium event statistics calculated from somatic areas of astrocytes reveal a frequency of about 1.2 transients per minute per region of interest (ROI), an amplitude of about 3 dF/F, and a duration of about 3–10 s although shorter and longer spontaneous calcium events can occur as well [53]. Similar values have been reported in [55] when using organotypic slices prepared from mice hippocampus and imaged by confocal microscopy. 0.17 transients per minute, with an average duration of about 10 s, have been shown in astrocytes using hippocampal slices [78]. Another study reveals that the overall pattern of calcium transients within astrocytes are similar between hippocampal astrocytes in brain slices and cortical astrocytes *in vivo* for wild type and $IP_3R2^{-/-}$ mice, implying that the measured calcium transients are not the consequence of the method employed to study them [53]. The exact statistics of calcium transients may vary depending on the brain area and developmental age [79], but [78] does not report differences with age. *In vivo*, spontaneous transients have had a frequency of 0.4 transients per minute per ROI in the soma and 0.64 transients per minute per ROI in the processes [80]. The amplitude of the transients varies from 0.1 dF/F in soma to about 0.35 dF/F in processes, and the average duration of the transients is about 10 s in both soma and processes [80]. Finally, Pirttimaki et al. [45] do not measure calcium dynamics directly, but the reported frequency of SIC currents is about 1.26 SIC/min and their duration is about 900 ms on average.

In our simulations, calcium transients appear with a frequency of about 0.1–1.5 transients per minute, with on average 0.5 transients per minute in asynchronous and on average 1.5 transients per minute in bursting regime. These transients last for about 1–10 s and increase from the baseline level below the concentration of 0.1 µM to at most 0.7 µM. All these values correspond well to the ranges seen across the experimental literature. However, the experimental values vary greatly across studies, experimental preparations, types of calcium transients, and astrocyte domains (soma vs processes). Systematic quantification of this diversity is lacking, and its functional role is unclear. Data-driven computational modeling of astrocytes would greatly benefit from systematic recordings of calcium transients and collecting sufficiently big and well documented benchmark data sets. Better categorization of calcium transients, their dynamic properties and functional roles is necessary. Finally, understanding calcium dynamics across astrocyte compartments is critical not only for advancing computational models of single astrocytes and neuron-astrocyte circuits, but also for understanding the role of astrocytes in brain systems in general.

We conduct an extensive parameter search to identify models that reproduce experimentally observed spontaneous calcium dynamics in astrocytes. The obtained optimal astrocyte model does not exhibit oscillatory dynamics, as this regime tends to produce too frequent and unrealistically regular calcium transients. Instead, in the best models, calcium transients are evoked by a low-frequency Poisson noise and are converging to the steady state without transients in the absence of noise inputs. Reproducing frequency, duration, and reasonable peak amplitudes of spontaneous calcium transients requires a low frequency of the input noise (about 4 spikes/s), relatively small time constant for IP_3 (τ_{IP_3} is about 1 s) and somewhat large IP_3 increment at each synaptic event (Δ_{IP_3} is about 0.05 µM). Simulations with active synaptic transmission require a reduction of the frequency of the input noise to about 70% of the fitted value to maintain similar levels of astrocyte inputs in the presence of synaptic glutamate processing. These fitted values likely reflect a rather simplified model of the IP_3 receptor that increases instantaneously at each synaptic event and decreases exponentially between events. A model with richer dynamics for both astrocytic IP_3 and calcium might be able to reproduce realistic spontaneous dynamics for a wider range of physiologically realistic model parameters.

We select the well-known depolarizing slow inward currents (SICs) as the first target of a technology for the representation of neuron-astrocyte interaction in large-scale neuronal network simulations. SIC currents occur in many different brain regions, including the hippocampus [13, 15–18, 20, 27, 81], the thalamus [14], various areas of the cerebral cortex [25, 26], the olfactory bulb [20], the nucleus accumbens [21], and the spinal cord [22, 23]. SIC currents are observed in both physiological and pathological conditions, using various preparations such as cell cultures and brain slices *in vitro*. The activation of SIC currents occurs primarily through the calcium-dependent release of glutamate from astrocytes, the mechanism, which we select to model and further study. The calcium-dependent release of glutamate from astrocytes has long been controversial (see e.g., [82, 83]). In 2023, however, it was convincingly shown that specialized astrocytes indeed mediate gliotransmission in the central nervous system and have molecular machinery to release glutamate in a calcium-dependent manner [9]. Alternative mechanisms such as glutamate release via ion channels may also exist to activate SIC currents [84]. The molecular details regarding the activation mechanisms of SIC currents remain an important future study area. SIC currents are observed in both mice and humans, but their significance appears to diminish with aging in humans (no or relatively little SIC currents were found in over 70-year-old humans) [50]. Overall, the functional role of SIC currents in the brain is not fully understood, highlighting the importance of developing computational brain models to better comprehend the role and function of SIC currents in the brain.

The computational model developed and analyzed in this study, a network model of spontaneous neuronal and astrocyte activity, focuses on a specific SIC-related function reported in the experimental literature [45, 47]. The use case model supports the emergence of synchronized spiking patterns in groups of neurons that interact with the same astrocyte. Our study confirms the result using two metrics, the first based on timing of successive SIC-induced bursts and the second based on standard pairwise correlation, and reproduces it in networks with two different interaction schemes, and under two global spiking activity regimes. The first confirmation comes from models with sparse asynchronous network activity regime, where each neuron receives inputs from only one astrocyte. However, the result also holds in models where neurons receive inputs from several astrocytes, and in both asynchronous regime (see Fig 12) and under network bursting (see Fig 6 in S3 Appendix). Switching from the asynchronous regime to network bursting is achieved by increasing the efficiency of interaction from neurons to astrocytes, which produces network bursts at the same frequency as astrocytic

calcium transients, around 0.1-1.5 bursts/min. Global network bursting increases synchronization between all neuronal pairs in the model (e.g. see Fig 10D and Fig 11D) which can mask the local SIC-induced synchrony in groups of neurons. However, under the given frequency of network bursting, the effect of SIC-induced synchrony is still evident. Further increase of the network bursting frequency increases global neuronal synchronization and ultimately masks the effect of SIC current. Additionally, in this study we consider a relatively small model, a network of 500 neurons and 100 astrocytes. Studying the role of this and similar mechanisms in realistic-size networks requires an efficient computational platform to tune the model to the desired global activity regime and simulate it for a long enough time to observe relatively slow (when compared to neuronal activity) changes in astrocyte dynamics. Our technology enables the future exploration of this and other similar mechanisms in realistic-size models. The functional role of this synchronicity inducing mechanism is unclear, but might be relevant in all functions that require coherent activation of neuronal groups, including for example plasticity or memory retrieval.

Reproducibility and future considerations

The traceability of model implementations is crucial, necessitating open accessibility, such as including codes in model databases and clarifying the evolutionary path from previously published models. To maintain the principles of FAIR (Findable, Accessible, Interoperable, and Reusable) data, the use of standardized simulation tools and data-analysis and sensitivity-analysis methodologies are necessary for all computational fields [85]. Advancing model development workflows and expanding neuroinformatics tools for astrocytes are crucial in enhancing reproducibility, standardization, and sharing of astrocyte models. To facilitate comprehensive specification, we recommend to employ a predefined format for describing model components and interaction schemes. In this regard, formats proposed for specifying neuronal networks [61] and connectivity schemes between neurons [64] can be expanded to accommodate neuron-astrocyte networks. All aspects of models, including network structure, cell count, interaction dynamics, and all the equations, initial and parameter values, must be explicitly disclosed as suggested recently [32]. The description of interaction schemes should seamlessly intertwine with model equations, ensuring that the reconstruction of these schemes is achievable solely through the equations [32]. All these advancements are crucial for expediting model development, adding greater biological knowledge into data-driven models, and integrating astrocytic mechanisms into large-scale, realistic models of brain systems. Our reference implementation for neuron-astrocyte networks helps to catalyze the development of neuron-astrocyte network models by providing fast simulation times and a reliable model implementation via the `TripartiteConnect()` concept, not present in other similar simulation tools.

Computational models and tools in brain research have become increasingly crucial in advancing our understanding of brain functions, dysfunctions, and diseases [86]. These allow researchers to simulate and analyze complex neural processes, providing valuable insights into the functioning of the brain and helping to solve the mysteries of neurological phenomena. They enable the exploration of various scenarios and aid in deciphering the underlying mechanisms of both normal brain function and aberrations leading to disorders. In addition, they facilitate the development of hypotheses and the testing of theories, offering possibilities for breakthroughs in neuroscience research.

Supporting information

S1 Appendix. Description of the neuron-astrocyte network models

S2 Appendix. Variables and parameters added to the NEST support for astrocytes

S3 Appendix. Selection of parameters for *in silico* model of neuron-astrocyte network

Author Contributions

Conceptualization: H-JJ, JA, TM, MD, SJvA, HEP, M-LL
Data curation: H-JJ, JA
Formal analysis: H-JJ, JA
Funding acquisition: JA, TM, MD, SJvA, HEP, M-LL
Investigation: H-JJ, JA, TM
Methodology: H-JJ, JA, TM, JS, ML, MD, SJvA, HEP, M-LL
Project administration: H-JJ, JA
Resources: MD, SJvA, HEP
Software: H-JJ, JA, TM, IA, JS, ML, HEP
Supervision: JA, MD, SJvA, HEP, M-LL
Validation: H-JJ, JA, TM, IA, JS, MD, SJvA, HEP, M-LL
Visualization: H-JJ, JA, TM, M-LL
Writing – original draft Preparation: H-JJ, JA, TM, JS, MD, HEP, M-LL
Writing – review & editing: H-JJ, JA, TM, IA, MD, SJvA, HEP, M-LL

Acknowledgments

We thank Dr. Tom Tetzlaff and Melissa Lober for the communication that allowed us to implement a surrogate model for the astrocyte, which is adapted from their implementation of the `ignore_and_fire` neuron model in NEST (personal communication). We thank Dr. David Dahmen for the consultation on the continuous interaction framework for `sic_connection`. We thank Dr. Noora Pihlajarinne for her work on panels in Fig 1 for the illustration of neuron-astrocyte interactions and Fig 1 in S2 Appendix for the illustration of software components required for the representation of the model and their embedding in the NEST code. We further thank Agnes Korcsak-Gorzo and Jose Villamar for help on the installation and workflow implementation with beNNch as well as Pooja Babu for her help in disseminating preliminary results of this work. Dr. Jugoslava Aćimović is currently employed as data scientist at AstraZeneca, however the research presented here was conducted during her previous employment at Tampere University and is unrelated to her current employment. Thus, her affiliation with Tampere University is used in this article.

References

1. Graber S, Mitchell J, Kurth AC, Terhorst D, Skaar JEW, Schöfmann CM, et al.. NEST 3.8; 2024. Available from: `https://doi.org/0.5281/zenodo.12624784`.

2. Bushong EA, Martone ME, Jones YZ, Ellisman MH. Protoplasmic astrocytes in CA1 stratum radiatum occupy separate anatomical domains. Journal of Neuroscience. 2002;22(1):183–192. doi:10.1523/JNEUROSCI.22-01-00183.2002.

3. Oberheim NA, Takano T, Han X, He W, Lin JHC, Wang F, et al. Uniquely hominid features of adult human astrocytes. Journal of Neuroscience. 2009;29(10):3276–3287. doi:10.1523/JNEUROSCI.4707-08.2009.

4. Vasile F, Dossi E, Rouach N. Human astrocytes: structure and functions in the healty brain. Brain Structure and Function. 2017;222:2017–2029. doi:10.1007/s00429-017-1383-5.

5. Calì C, Agus M, Kare K, Boges DJ, Lehväslaiho H, Hadwiger M, et al. 3D cellular reconstruction of cortical glia and parenchymal morphometric analysis from Serial Block-Face Electron Microscopy of juvenile rat. Progress in Neurobiology. 2019;183:101696. doi:10.1016/j.pneurobio.2019.101696.

6. Kikuchi T, Gonzalez-Soriano J, Kastanauskaite A, Benavides-Piccione R, Merchan-Perez A, DeFelipe J, et al. Volume electron microscopy study of the relationship between synapses and astrocytes in the developing rat somatosensory cortex. Cerebral Cortex. 2020;30(6):3800–3819. doi:10.1093/cercor/bhz343.

7. Zisis E, Keller D, Kanari L, Arnaudon A, Gevaert M, Delemontex T, et al. Digital reconstruction of the neuro-glia-vascular architecture. Cerebral Cortex. 2021;31(12):5686–5703. doi:10.1093/cercor/bhab254.

8. Aten S, Kiyoshi CM, Arzola EP, Patterson JA, Taylor AT, Du Y, et al. Ultrastructural view of astrocyte arborization, astrocyte-astrocyte and astrocyte-synapse contacts, intracellular vesicle-like structures, and mitochondrial network. Progress in Neurobiology. 2022;213:102264. doi:10.1016/j.pneurobio.2022.102264.

9. de Ceglia R, Ledonne A, Litvin DG, Lind BL, Carriero G, Latagliata EC, et al. Specialized astrocytes mediate glutamatergic gliotransmission in the CNS. Nature. 2023;622(7981):120–129. doi:10.1038/s41586-023-06502-w.

10. Araque A, Parpura V, Sanzgiri RP, Haydon PG. Tripartite synapses: glia, the unacknowledged partner. Trends in Neurosciences. 1999;22(5):208–215. doi:10.1016/S0166-2236(98)01349-6.

11. Parpura V, Basarsky TA, Liu F, Jeftinija K, Jeftinija S, Haydon PG. Glutamate-mediated astrocyte–neuron signalling. Nature. 1994;369:744–747. doi:10.1038/369744a0.

12. Navarrete M, Perea G, de Sevilla DF, Gómez-Gonzalo M, Núñez A, Martín ED, et al. Astrocytes mediate in vivo cholinergic-induced synaptic plasticity. PLoS Biology. 2012;10(2):e1001259. doi:10.1371/journal.pbio.1001259.

13. Araque A, Parpura V, Sanzgiri RP, Haydon PG. Glutamate-dependent astrocyte modulation of synaptic transmission between cultured hippocampal neurons. European Journal of Neuroscience. 1998;10:2129–2142. doi:10.1046/j.1460-9568.1998.00221.x.

14. Parri HR, Gould TM, Crunelli V. Spontaneous astrocytic Ca^{2+} oscillations in situ drive NMDAR-mediated neuronal excitation. Nature Neuroscience. 2001;4(8):803–812. doi:10.1038/90507.

15. Angulo MC, Kozlov AS, Charpak S, Audinat E. Glutamate released from glial cells synchronizes neuronal activity in the hippocampus. Journal of Neuroscience. 2004;24(31):6920–6927. doi:10.1523/JNEUROSCI.0473-04.2004.

16. Fellin T, Pascual O, Gobbo S, Pozzan T, Haydon PG, Carmignoto G. Neuronal synchrony mediated by astrocytic glutamate through activation of extrasynaptic NMDA receptors. Neuron. 2004;43(5):729–743. doi:10.1016/j.neuron.2004.08.011.

17. Perea G, Araque A. Properties of synaptically evoked astrocyte calcium signal reveal synaptic information processing by astrocytes. Journal of Neuroscience. 2005;25(9):2192–2203. doi:10.1523/JNEUROSCI.3965-04.2005.

18. Carmignoto G, Fellin T. Glutamate release from astrocytes as a non-synaptic mechanism for neuronal synchronization in the hippocampus. Journal of Physiology (Paris). 2006;99(2-3):98–102. doi:10.1016/j.jphysparis.2005.12.008.

19. Gao WJ, Goldman-Rakic PS. NMDA receptor-mediated epileptiform persistent activity requires calcium release from intracellular stores in prefrontal neurons. Experimental Neurology. 2006;197(2):495–504. doi:10.1016/j.expneurol.2005.05.018.

20. Kozlov AS, Angulo MC, Audinat E, Charpak S. Target cell-specific modulation of neuronal activity by astrocytes. Proceedings of the National Academy of Sciences of the United States of America. 2006;103(26):10058–10063. doi:10.1073/pnas.0603741103.

21. D'Ascenzo M, Fellin T, Terunuma M, Revilla-Sanchez R, Meaney DF, Auberson YP, et al. mGluR5 stimulates gliotransmission in the nucleus accumbens. Proceedings of the National Academy of Sciences of the United States of America. 2007;104(6):1995–2000. doi:10.1073pnas.0609408104.

22. Bardoni R, Ghirri A, Zonta M, Betelli C, Vitale G, Ruggieri V, et al. Glutamate-mediated astrocyte-to-neuron signalling in the rat dorsal horn. Journal of Physiology. 2010;588(5):831–846. doi:10.1113/jphysiol.2009.180570.

23. Nie H, Zhang H, Weng HR. Bidirectional neuron–glia interactions triggered by deficiency of glutamate uptake at spinal sensory synapses. Journal of Neurophysiology. 2010;104(2):713–725. doi:10.1152/jn.00282.2010.

24. Reyes-Haro D, Müller J, Boresch M, Pivneva T, Benedetti B, Scheller A, et al. Neuron–astrocyte interactions in the medial nucleus of the trapezoid body. Journal of General Physiology. 2010;135(6):583–594. doi:10.1085/jgp.200910354.

25. Chen N, Sugihara H, Sharma J, Perea G, Petravicz J, Le C, et al. Nucleus basalis-enabled stimulus-specific plasticity in the visual cortex is mediated by astrocytes. Proceedings of the National Academy of Sciences of the United States of America. 2012;109(41):E2832–E2841. doi:10.1073/pnas.1206557109.

26. Perea G, Yang A, Boyden ES, Sur M. Optogenetic astrocyte activation modulates response selectivity of visual cortex neurons *in vivo*. Nature Communications. 2014;5:3262. doi:10.1038/ncomms4262.

27. Lauderdale K, Murphy T, Tung T, Davila D, Binder DK, Fiacco TA. Osmotic edema rapidly increases neuronal excitability through activation of NMDA receptor-dependent slow inward currents in juvenile and adult hippocampus. ASN Neuro. 2015;7(5):1–12. doi:10.1177/1759091415605115.

28. Navarrete M, Perea G, Maglio L, Pastor J, de Sola RG, Araque A. Astrocyte calcium signal and gliotransmission in human brain tissue. Cerebral Cortex. 2013;23:1240–1246. doi:10.1093/cercor/bhs122.

29. Manninen T, Aćimović J, Havela R, Teppola H, Linne ML. Challenges in reproducibility, replicability, and comparability of computational models and tools for neuronal and glial networks, cells, and subcellular structures. Frontiers in Neuroinformatics. 2018;12:20. doi:10.3389/fninf.2018.00020.

30. Manninen T, Havela R, Linne ML. Computational models for calcium-mediated astrocyte functions. Frontiers in Computational Neuroscience. 2018;12:14. doi:10.3389/fncom.2018.00014.

31. Manninen T, Havela R, Linne ML. Computational models of astrocytes and astrocyte-neuron interactions: characterization, reproducibility, and future perspectives. In: De Pittà M, Berry H, editors. Computational Glioscience. Cham, Switzerland: Springer; 2019. p. 423–454.

32. Manninen T, Aćimović J, Linne ML. Analysis of network models with neuron-astrocyte interactions. Neuroinformatics. 2023;21:375–406. doi:10.1007/s12021-023-09622-w.

33. Linne ML, Aćimović J, Saudargiene A, Manninen T. Neuron–glia interactions and brain circuits. In: Giugliano M, Negrello M, Linaro D, editors. Computational Modelling of the Brain: Modelling Approaches to Cells, Circuits and Networks. Cham, Switzerland: Springer; 2022. p. 87–103.

34. Gewaltig MO, Diesmann M. NEST (neural simulation tool). Scholarpedia. 2007;2(4):1430.

35. Potjans TC, Diesmann M. The cell-type specific cortical microcircuit: relating structure and activity in a full-scale spiking network model. Cerebral Cortex. 2014;24(3):785–806. doi:10.1093/cercor/bhs358.

36. Schmidt M, Bakker R, Shen K, Bezgin G, Diesmann M, van Albada SJ. A multi-scale layer-resolved spiking network model of resting-state dynamics in macaque visual cortical areas. PLoS Computational Biology. 2018;14(10):e1006359. doi:10.1371/journal.pcbi.1006359.

37. Aleksin SG, Zheng K, Rusakov DA, Savtchenko LP. ARACHNE: a neural-neuroglial network builder with remotely controlled parallel computing. PLoS Computational Biology. 2017;13(3):e1005467. doi:10.1371/journal.pcbi.1005467.

38. Stimberg M, Brette R, Goodman DFM. Brian 2, an intuitive and efficient neural simulator. eLife. 2019;8:e47314. doi:10.7554/eLife.47314.

39. Stimberg M, Goodman DFM, Brette R, De Pittà M. Modeling neuron–glia interactions with the Brian 2 simulator. In: De Pittà M, Berry H, editors. Computational Glioscience. Cham, Switzerland: Springer; 2019. p. 471–505.

40. De Young GW, Keizer J. A single-pool inositol 1,4,5-trisphosphate-receptor-based model for agonist-stimulated oscillations in Ca^{2+} concentration. Proceedings of the National Academy of Sciences of the United States of America. 1992;89(20):9895–9899. doi:10.1073/pnas.89.20.9895.

41. Li YX, Rinzel J. Equations for $InsP_3$ receptor-mediated $[Ca^{2+}]_i$ oscillations derived from a detailed kinetic model: a Hodgkin-Huxley like formalism. Journal of Theoretical Biology. 1994;166(4):461–473. doi:10.1006/jtbi.1994.1041.

42. Nadkarni S, Jung P. Spontaneous oscillations of dressed neurons: a new mechanism for epilepsy? Physical Review Letters. 2003;91(26):268101. doi:10.1103/PhysRevLett.91.268101.

43. Allegrini P, Fronzoni L, Pirino D. The influence of the astrocyte field on neuronal dynamics and synchronization. Journal of Biological Physics. 2009;35(4):413–423. doi:10.1007/s10867-009-9166-8.

44. Liu Y, Li C. Firing rate propagation through neuronal–astrocytic network. IEEE Transactions on Neural Networks and Learning Systems. 2013;24(5):789–799. doi:10.1109/TNNLS.2013.2245678.

45. Pirttimaki TM, Sims RE, Saunders G, Antonio SA, Codadu NK, Parri HR. Astrocyte-mediated neuronal synchronization properties revealed by false gliotransmitter release. Journal of Neuroscience. 2017;37(41):9859–9870. doi:10.1523/JNEUROSCI.2761-16.2017.

46. Lines J, Martin ED, Kofuji P, Aguilar J, Araque A. Astrocytes modulate sensory-evoked neuronal network activity. Nature Communications. 2020;11:3689. doi:10.1038/s41467-020-17536-3.

47. Pirttimaki TM, Hall SD, Parri HR. Sustained neuronal activity generated by glial plasticity. Journal of Neuroscience. 2011;31(21):7637–7647. doi:10.1523/JNEUROSCI.5783-10.2011.

48. Wetherington J, Serrano G, Dingledine R. Astrocytes in the epileptic brain. Neuron. 2008;58(2):168–178. doi:10.1016/j.neuron.2008.04.002.

49. Dong QP, He JQ, Chai Z. Astrocytic Ca^{2+} waves mediate activation of extrasynaptic NMDA receptors in hippocampal neurons to aggravate brain damage during ischemia. Neurobiology of Disease. 2013;58:68–75. doi:10.1016/j.nbd.2013.05.005.

50. Csemer A, Kovács A, Maamrah B, Pocsai K, Korpás K, Klekner Á, et al. Astrocyte- and NMDA receptor-dependent slow inward currents differently contribute to synaptic plasticity in an age-dependent manner in mouse and human neocortex. Aging Cell. 2023;22(9):e13939. doi:10.1111/acel.13939.

51. Kovács A, Pál B. Astrocyte-dependent slow inward currents (SICs) participate in neuromodulatory mechanisms in the pedunculopontine nucleus (PPN). Frontiers in Cellular Neuroscience. 2017;11:16. doi:10.3389/fncel.2017.00016.

52. Pirttimaki TM, Parri HR. Glutamatergic input–output properties of thalamic astrocytes. Neuroscience. 2012;205:18–28. doi:10.1016/j.neuroscience.2011.12.049.

53. Srinivasan R, Huang BS, Venugopal S, Johnston AD, Chai H, Zeng H, et al. Ca^{2+} signaling in astrocytes from $Ip3r2^{-/-}$ mice in brain slices and during startle responses *in vivo*. Nature Neuroscience. 2015;18(5):708–717. doi:10.1038/nn.4001.

54. Stobart JL, Ferrari KD, Barrett MJP, Glück C, Stobart MJ, Zuend M, et al. Cortical circuit activity evokes rapid astrocyte calcium signals on a similar timescale to neurons. Neuron. 2018;98(4):726–735. doi:10.1016/j.neuron.2018.03.050.

55. Arizono M, Inavalli VVG, Panatier A, Pfeiffer T, Angibaud J, Levet F, et al. Structural basis of astrocytic Ca^{2+} signals at tripartite synapses. Nature Communications. 2020;11(1):1906. doi:10.1038/s41467-020-15648-4.

56. Aćimović J, Jiang HJ, Manninen T, Stapmanns J, Lehtimäki M, Linne ML, et al. The NEST module for computational modeling of neuron-astrocyte networks. In: Proceedings of Annual Computational Neuroscience Meeting. Leipzig, Germany; 2023.

57. Jiang HJ, Aćimović J, Manninen T, Stapmanns J, Lehtimäki M, Linne ML, et al. Computational modelling of neuron-astrocyte interactions in the NEST simulator. In: Proceedings of Göttingen Meeting of the German Neuroscience Society. Göttingen, Germany; 2023.

58. Villamar J, Vogelsang J, Linssen C, Kunkel S, Kurth A, Schöfmann CM, et al.. NEST 3.6; 2023. Available from: `https://doi.org/10.5281/zenodo.8344932`.

59. Espinoza Valverde JA, Müller E, Haug N, Schöfmann CM, Linssen C, Senk J, et al.. NEST 3.7; 2024. Available from: `https://dx.doi.org/10.5281/zenodo.10834751`.

60. Plesser HE. Astrocyte Surrogate Module; 2024. Available from: `https://github.com/heplesser/astrocyte-surrogate-module`.

61. Nordlie E, Gewaltig MO, Plesser HE. Towards reproducible descriptions of neuronal network models. PLoS Computational Biology. 2009;5(8):e1000456. doi:10.1371/journal.pcbi.1000456.

62. Brette R, Gerstner W. Adaptive exponential integrate-and-fire model as an effective description of neuronal activity. Journal of Neurophysiology. 2005;94:3637–3642. doi:10.1152/jn.00686.2005.

63. Naud R, Marcille M, Clopath C, Gerstner W. Firing patterns in the adaptive exponential integrate-and-fire model. Biological Cybernetics. 2008;99:335–347. doi:10.1007/s00422-008-0264-7.

64. Senk J, Kriener B, Djurfeldt M, Voges N, Jiang HJ, Schüttler L, et al. Connectivity concepts in neuronal network modeling. PLoS Computational Biology. 2022;18(9):e1010086. doi:10.1371/journal.pcbi.1010086.

65. Milo R, Shen-Orr S, Itzkovitz S, Kashtan N, Chklovskii D, Alon U. Network motifs: simple building blocks of complex networks. Science (New York, NY). 2002;298(5594):824–827. doi:doi.org/10.1126/science.298.5594.824.

66. Pernice V, Staude B, Cardanobile S, Rotter S. How structure determines correlations in neuronal networks. PLoS computational biology. 2011;7(5):e1002059. doi:doi.org/10.1371/journal.pcbi.1002059.

67. Aćimović J, Mäki-Marttunen T, Linne ML. The effects of neuron morphology on graph theoretic measures of network connectivity: The analysis of a two-level statistical model. Frontiers in Neuroanatomy. 2015;9. doi:10.3389/fnana.2015.00076.

68. Jovanović S, Rotter S. Interplay between Graph Topology and Correlations of Third Order in Spiking Neuronal Networks. PLOS Computational Biology. 2016;12(6):1–28. doi:10.1371/journal.pcbi.1004963.

69. Morrison A, Mehring C, Geisel T, Aertsen A, Diesmann M. Advancing the boundaries of high connectivity network simulation with distributed computing. Neural Computation. 2005;17:1776–1801. doi:10.1162/0899766054026648.

70. Plesser HE, Eppler JM, Morrison A, Diesmann M, Gewaltig MO. Efficient Parallel Simulation of Large-Scale Neuronal Networks on Clusters of Multiprocessor Computers. In: Kermarrec AM, Bougé L, Priol T, editors. Euro-Par 2007: Parallel Processing. vol. 4641 of Lecture Notes in Computer Science. Berlin: Springer-Verlag; 2007. p. 672–681.

71. Jordan J, Ippen T, Helias M, Kitayama I, Sato M, Igarashi J, et al. Extremely scalable spiking neuronal network simulation code: From laptops to exascale computers. Frontiers in Neuroinformatics. 2018;12:2. doi:10.3389/fninf.2018.00002.

72. Albers J, Pronold J, Kurth AC, Vennemo SB, Mood KH, Patronis A, et al. A modular workflow for performance benchmarking of neuronal network simulations. Frontiers in Neuroinformatics. 2022;16:837549. doi:10.3389/fninf.2022.837549.

73. Neske GT, Patrick SL, Connors BW. Contributions of diverse excitatory and inhibitory neurons to recurrent network activity in cerebral cortex. Journal of Neuroscience. 2015;35(3):1089–1105. doi:10.1523/JNEUROSCI.2279-14.2015.

74. Sun QQ, Huguenard JR, Prince DA. Barrel cortex microcircuits: thalamocortical feedforward inhibition in spiny stellate cells is mediated by a small number of fast-spiking interneurons. Journal of Neuroscience. 2006;26(4):1219–1230. doi:10.1523/JNEUROSCI.4727-04.2006.

75. Touboul J, Brette R. Dynamics and bifurcations of the adaptive exponential integrate-and-fire model. Biological Cybernetics. 2008;99:319–334. doi:10.1007/s00422-008-0267-4.

76. Hahne J, Helias M, Kunkel S, Igarashi J, Bolten M, Frommer A, et al. A unified framework for spiking and gap-junction interactions in distributed neuronal network simulations. Frontiers in Neuroinformatics. 2015;9:22. doi:10.3389/fninf.2015.00022.

77. De Pittà M, Brunel N. Multiple forms of working memory emerge from synapse–astrocyte interactions in a neuron–glia network model. Proceedings of the National Academy of Sciences of the United States of America. 2022;119(43):e2207912119. doi:10.1073/pnas.2207912119.

78. Sasaki T, Kuga N, Namiki S, Matsuki N, Ikegaya Y. Locally synchronized astrocytes. Cerebral Cortex. 2011;21(8):1889–1900. doi:10.1093/cercor/bhq256.

79. Nakayama R, Sasaki T, Tanaka KF, Ikegaya Y. Subcellular calcium dynamics during juvenile development in mouse hippocampal astrocytes. European Journal of Neuroscience. 2016;43(7):923–932. doi:10.1111/ejn.13188.

80. Stobart JL, Ferrari KD, Barrett MJP, Stobart MJ, Looser ZJ, Saab AS, et al. Long-term in vivo calcium imaging of astrocytes reveals distinct cellular compartment responses to sensory stimulation. Cerebral Cortex. 2018;28(1):184–198. doi:10.1093/cercor/bhw366.

81. Araque A, Sanzgiri RP, Parpura V, Haydon PG. Calcium elevation in astrocytes causes an NMDA receptor-dependent increase in the frequency of miniature synaptic currents in cultured hippocampal neurons. Journal of Neuroscience. 1998;18(17):6822–6829. doi:10.1523/JNEUROSCI.18-17-06822.1998.

82. Fiacco TA, McCarthy KD. Multiple lines of evidence indicate that gliotransmission does not occur under physiological conditions. Journal of Neuroscience. 2018;38(1):3–13. doi:10.1523/JNEUROSCI.0016-17.2017.

83. Savtchouk I, Volterra A. Gliotransmission: beyond black-and-white. Journal of Neuroscience. 2018;38(1):14–25. doi:10.1523/JNEUROSCI.0017-17.2017.

84. Gómez-Gonzalo M, Zehnder T, Requie LM, Bezzi P, Carmignoto G. Insights into the release mechanism of astrocytic glutamate evoking in neurons NMDA receptor-mediated slow depolarizing inward currents. Glia. 2018;66(10):2188–2199. doi:10.1002/glia.23473.

85. Eriksson O, Bhalla US, Blackwell KT, Crook SM, Keller D, Kramer A, et al. Combining hypothesis- and data-driven neuroscience modeling in FAIR workflows. eLife. 2022;11:e69013. doi:10.7554/eLife.69013.

86. Amunts K, Axer M, Banerjee S, Bitsch L, Bjaalie JG, Brauner P, et al. The coming decade of digital brain research: A vision for neuroscience at the intersection of technology and computing. Imaging Neuroscience. 2024;2:1–35. doi:10.1162/imag_a_00137.